The Astronomical Journal, 148:107 (16pp), 2014 December doi:10.1088/0004-6256/148/6/107

PHOTOSPHERIC MAGNITUDE DIAGRAMS FOR TYPE II SUPERNOVAE: A PROMISING TOOL TO COMPUTE DISTANCES

Ósmar Rodríguez[1,2], Alejandro Clocchiatti[1,2], and Mario Hamuy[1,3]
[1] Millennium Institute of Astrophysics, Casilla 36-D, Santiago, Chile
[2] Instituto de Astrofísica, Facultad de Física, Pontificia Universidad Católica de Chile, Casilla 306, Santiago 22, Chile; olrodrig@astro.puc.cl
[3] Departamento de Astronomía, Universidad de Chile, Casilla 36-D, Santiago, Chile
Received 2014 June 15; accepted 2014 August 10; published 2014 October 30

ABSTRACT

We develop an empirical color-based standardization for Type II supernovae (SNe II), equivalent to the classical surface brightness method given in Wesselink. We calibrate this standardization using SNe II with host galaxy distances measured using Cepheids, and a well-constrained shock breakout epoch and extinction due to the host galaxy. We estimate the reddening with an analysis of the $B-V$ versus $V-I$ color–color curves, similar to that of Natali et al. With four SNe II meeting the above requirements, we build a photospheric magnitude versus color diagram (similar to an H-R diagram) with a dispersion of 0.29 mag. We also show that when using time since shock breakout instead of color as the independent variable, the same standardization gives a dispersion of 0.09 mag. Moreover, we show that the above time-based standardization corresponds to the generalization of the standardized candle method of Hamuy & Pinto for various epochs throughout the photospheric phase. To test the new tool, we construct Hubble diagrams for different subsamples of 50 low-redshift ($cz < 10^4$ km s^{-1}) SNe II. For 13 SNe within the Hubble flow ($cz_{\rm CMB} > 3000$ km s^{-1}) and with a well-constrained shock breakout epoch we obtain values of 68–69 km s^{-1} Mpc^{-1} for the Hubble constant and a mean intrinsic scatter of 0.12 mag or 6% in relative distances.

Key words: distance scale – galaxies: distances and redshifts – supernovae: general

1. INTRODUCTION

Core–collapse supernovae (SNe) are recognized as the final stage of stars with an initial mass $\gtrsim 8\,M_\odot$ characterized by their great luminosities, comparable to the total luminosity of their host galaxies, and a sustained growth in size (an envelope ejection) due to the energy released by the gravitational collapse of the iron core (e.g., Burrows 2000). Among these SNe, many show evidence for hydrogen (H) in their spectra, being historically classified as Type II (Minkowski 1941). For this spectral type, Barbon et al. (1979) proposed a subclassification based on the shape of the light curve during the photospheric phase, i.e., the stage between maximum light and the transition to the radioactive tail: Type II "plateau" (II-P) for those SNe that display a nearly constant optical luminosity during ∼100 days and Type II "linear" (II-L) for those that show a linearly declining luminosity. Two other subclasses have been introduced based on spectral characteristics: IIn for SNe that show narrow H emission lines (Schlegel 1990), and IIb for those that show H in early spectra that soon disappear (Woosley et al. 1987). Finally, a few SNe do not fit into the aforementioned subclasses, but show characteristics similar to SN 1987A (e.g., Kleiser et al. 2011; Taddia et al. 2012; Pastorello et al. 2012). More recently, Anderson et al. (2014) performed a photometric analysis of a sample of 116 SNe II. They did not find a clear separation between II-P and II-L subclasses, so they proposed a continuous subclass, named simply "II," where each SN is characterized by the decline rate during the plateau phase. Core–collapse SNe are the most frequent of all SNe (76% belonging to this class; Li et al. 2011), with SNe II (II-P and II-L) being the most frequent among core–collapse events (∼55%; Smith et al. 2011).

The physics of radiative transfer during the photospheric phase of SNe II-P is the better understood and probably the easiest to model for SN theorists (e.g., Eastman et al. 1996; Dessart & Hillier 2005). The above is further strengthened by the clear identification of red supergiants as progenitors of SNe II-P, which is fundamental to consolidating the hypothesis of a core–collapse process (Smartt 2009). All these characteristics (i.e., high luminosity, high relative frequency, and physical understanding of the phenomenon) make SNe II-P well suited for in-depth study and interesting for distance measurement.

At present, thermonuclear (Ia) SNe are a more mature astrophysical tool for measuring distances: they are ∼1–2 mag brighter than SNe II-P in the optical and have been shown to display the highest degree of both photometric and spectroscopic homogeneity (Li et al. 2001). Type Ia SNe are not perfect standard candles, but empirical calibrations have allowed us to standardize their luminosities with a dispersion in absolute magnitude of ∼0.15–0.22 mag and therefore to determine distances to their host galaxies with an unprecedented precision of ∼7%–10% (Phillips 1993; Hamuy et al. 1996; Phillips et al. 1999).

First attempts to measure distances to SNe II assume that these phenomena emit as blackbodies (e.g., Kirshner & Kwan 1974). However, the scattering-dominated atmospheres of SNe II are not well suited for the simple blackbody approximation (Wagoner 1981), and this becomes an important factor to consider in distance measurements. Proposed solutions come from theoretical approaches to SN II atmospheres by Eastman et al. (1996) and Dessart & Hillier (2005). However, significant systematic discrepancies exist between these two sets of models, leading to ∼50% differences in distances (Jones et al. 2009).

To get around this problem, empirical methods have been developed to estimate distances to SNe II (e.g., Hamuy & Pinto 2002), but they do not make full use of the SNe II-P simplified model physics. Therefore, on the one hand we have theory-based methods with conflicting results, and on the other hand, empirical methods that work well but do not make full use of the possibilities of the underlying simple model.

The goal of this research is to take advantage of the simplified physics of SNe II to find improved ways of estimating distances.

We organize our work as follows. In Section 2 we describe the photometric and spectroscopic data. In Section 3 we develop the standard framework and a standardization based on color is presented in Section 3.2. In Section 4 we discuss some crucial parameters involved in our analysis with emphasis on the development of a method for measuring host galaxy extinction in Section 4.1. In Section 5 we show our results: extinction measurements, the color-based standardization, and an alternative standardization based on time since shock breakout. In Section 6 we discuss some aspects of the classical surface brightness method (SBM) and the next refinement steps for the method proposed in this work. We present our conclusions in Section 7.

2. OBSERVATIONAL MATERIAL

We base our work on data obtained over the course of four different systematic SN follow-up programs: the Cerro Tololo SN program (PIs: Phillips and Suntzeff, 1986–2003), the Calán/Tololo SN survey (PI: Hamuy, 1989–1993), the Supernova Optical and Infrared Survey (SOIRS; PI: Hamuy, 1999–2000), and the Carnegie Type II Supernova Survey (CATS; PI: Hamuy, 2002–2003). The data were obtained with telescopes from Cerro Tololo Inter-American Observatory, Las Campanas Observatory, the European Southern Observatory (ESO) in La Silla, and Steward Observatory. Details on the telescope–instrument combinations are provided in Jones (2008). The four programs obtained optical (and some IR) photometry and spectroscopy for nearly 100 SNe of all types, 47 of which belong to the Type II class (excluding IIn, IIb, and 1987A-like events). All of the optical data and the detailed description of the instruments used and the data reduction methods are being prepared for publication. Next we briefly summarize the general techniques used to obtain the photometric and spectroscopic data.

2.1. Photometric Data

The photometric observations were carried out with the Johnson–Kron–Cousins–Hamuy *UBVRIZ* broadband filters (Johnson et al. 1966; Cousins 1971; Hamuy et al. 2001). The images were processed with IRAF[4] through bias subtraction and flat-field correction. All of them were further processed through host galaxy subtraction using template images of the host galaxies. Photometric sequences were established around each SN based on observations of Landolt and Hamuy flux standard stars (Landolt 1992; Hamuy et al. 1992, 1994). The photometry of all SNe was performed differentially with respect to the local sequence on the galaxy-subtracted images. The transformation of instrumental magnitudes into the standard system was done by taking into account a linear color term and a zero point.

2.2. Spectroscopic Data

Low resolution ($R \sim 1000$) optical spectra (wavelength range ~3200–10000 Å) were taken for each SN followed by comparison lamp spectra taken at the same position in the sky, and 2–3 flux standard stars per night from the list of Hamuy et al. (1992, 1994). Most of the spectra were taken with the slit along the parallactic angle (Filippenko et al. 1982). The reductions were performed with IRAF and consisted of bias subtraction, flat-field correction, one-dimensional spectrum extraction and sky subtraction, wavelength calibration, and flux calibration.

2.3. Sample of Supernovae

Among the 47 SNe II observed over the course of the four surveys, a subset of 33 objects complies with the requirements of (1) having photometry in *BVI* bands covering the photospheric phase, (2) having at least one measurement of expansion velocity, and (3) having redshifts lower than 10^4 km s^{-1} (see Section 3.3). To this sample, we added 17 SNe II from the literature[5]: SN 1999gi, SN 2001X, SN 2003Z, SN 2003gd, SN 2004A, SN 2004dj, SN 2004et, SN 2005ay, SN 2005cs, SN 2008in, SN 2009N, SN 2009bw, SN 2009js, SN 2009md, SN 2012A, SN 2012aw, and SN 2013ej. Spectroscopy of SN 2008in and SN 2009N is taken from the Carnegie Supernova Project (CSP; Hamuy et al. 2006). We also added the spectroscopy of SN 1999em published by Leonard et al. (2002a) and the spectroscopy of SN 2013ej obtained by C. Buil.[6] Table 1 summarizes our final sample of 50 SNe II, which includes the name of the host galaxy, the heliocentric redshift, the reddening due to our Galaxy (Schlafly & Finkbeiner 2011), the old SN subclassification (II-P or II-L) based on the *B*-band decline rate (β^B_{100}) criterion given in Patat et al. (1994), and the survey or references for the data.

3. TOOLS FOR MEASURING DISTANCES

For the sake of simplicity, we assume an SN with a spherically symmetric expanding photosphere that radiates isotropically. We choose to work with photon flux instead of energy flux due to the fact that observations are obtained with photon detectors.

3.1. Standard Framework

In the relation between distance and photon flux, for the general case of an SN in a galaxy at redshift z within the Hubble flow, we need to take into account the effects of the universe expansion. Photon wavelengths are stretched and the time is dilated, both by a factor $(1+z)$. Using the i subindex to indicate quantities at a given time t_i, and distinguishing between the observer's frame (unprimed) and the SN restframe (primed), we will have

$$\lambda' = \lambda/(1+z), \tag{1}$$

and

$$n_{\lambda,i} = \mathcal{N}_{\lambda',i}\left(\frac{R'_{\mathrm{ph},i}}{D_L}\right)^2 10^{-0.4(A_h(\lambda')+A_G(\lambda))}. \tag{2}$$

Here, n_λ is the monochromatic photon flux (in photons cm^{-2} s^{-1} Å^{-1}) measured by a local observer from an SN at luminosity distance D_L, with an emergent photon flux $\mathcal{N}_{\lambda'}$ emitted from the photosphere with radius R'_{ph}, affected by dust extinction in the host galaxy $A_h(\lambda')$ and our Galaxy $A_G(\lambda)$.

In terms of broadband fluxes, Equation (2) can be expressed as

$$\begin{aligned} m_{\bar{\lambda},i} &\equiv -2.5\log\int d\lambda S_{\bar{\lambda}}(\lambda) n_{\lambda,i} + \mathrm{ZP}_{\bar{\lambda}} \\ &= 5\log\left(\frac{D_L}{R'_{\mathrm{ph},i}}\right) + \widetilde{\mathcal{M}}_{\bar{\lambda},i}(A_G, z, A_h), \end{aligned} \tag{3}$$

[4] IRAF is distributed by the National Optical Astronomy Observatory, which is operated by the Association of Universities for Research in Astronomy (AURA) under cooperative agreement with the National Science Foundation.

[5] Spectroscopy for most of these SNe is available via WISeREP (http://www.weizmann.ac.il/astrophysics/wiserep/; Yaron & Gal-Yam 2012).

[6] http://www.astrosurf.com/buil/

Table 1
SN II Sample

SN Name	Host Galaxy	$cz_{\rm helio}$[a] (km s^{-1})	Source[b]	$E(B-V)_{\rm Gal}$[c] (mag)	Type	References
1991al	Anon	4572	H01	0.0438	II-L	1
1992af	ESO 340–G38	5517	Here	0.0449	II-P	1
1992ba	NGC 2082	1052	Here	0.0502	II-P	1
1993A	2MASX J07391822–6203095	8707	Here	0.1515	II-P	1
1993S	2MASX J22522390–4018432	9623	Here	0.0129	II-L	1
1999br	NGC 4900	874	Here	0.0203	II-P	2
1999ca	NGC 3120	2791	NED	0.0939	II-L	2
1999cr	ESO 576–G34	6050	Here	0.0846	II-P	2
1999eg	IC 1861	6703	NED	0.1014	II-L	2
1999em	NGC 1637	800	L02a	0.0349	II-P	2, 3
1999gi	NGC 3184	503	Here	0.0144	II-P	4
2001X	NGC 5921	1480	NED	0.0342	II-P	5, 6[d]
2002ew	NEAT J205430.50–000822.0	8834	Here	0.0882	II-L	7
2002gd	NGC 7537	2453	Here	0.0575	II-P	7
2002gw	NGC 992	3059	Here	0.0165	II-P	7
2002hj	NPM1G +04.0097	6994	Here	0.0992	II-P	7
2002hx	2MASX J08273975–1446551	9214	Here	0.0460	II-P	7
2003B	NGC 1097	1058	Here	0.0232	II-P	7
2003E	MCG –04–12–004	4400	Here	0.0417	II-P	7
2003T	UGC 4864	8368	NED	0.0272	II-P	7
2003Z	NGC 2742	1289	NED	0.0335	II-P	8
2003bl	NGC 5374	4211	Here	0.0232	II-P	7
2003bn	2MASX J10023529–2110531	3813	Here	0.0563	II-P	7
2003ci	UGC 6212	8967	Here	0.0508	II-L	7
2003cn	IC 849	5430	NED	0.0184	II-P	7
2003ef	NGC 4708	4093	Here	0.0395	II-P	7
2003ej	UGC 7820	5056	Here	0.0167	II-L	7
2003fb	UGC 11522	5081	Here	0.1559	II-P	7
2003gd	NGC 628	657	NED	0.0604	II-P	7, 9
2003hg	NGC 7771	4186	Here	0.0631	II-P	7
2003hk	NGC 1085	6880	Here	0.0313	II-L	7
2003hl	NGC 772	2123	Here	0.0624	II-P	7
2003hn	NGC 1448	1168	NED	0.0122	II-P	7
2003ho	ESO 235–G58	4091	Here	0.0339	II-P	7
2003ib	MCG –04–48–015	7442	NED	0.0418	II-P	7
2003ip	UGC 327	5398	NED	0.0564	II-L	7
2003iq	NGC 772	2331	Here	0.0624	II-P	7
2004A	NGC 6207	852	NED	0.0131	II-P	10, 11, 12
2004dj	NGC 2403	221	V06	0.0344	II-P	13, 14
2004et	NGC 6946	40	NED	0.2937	II-P	15, 16
2005ay	NGC 3938	809	NED	0.0183	II-P	17, 6[d]
2005cs	NGC 5194	463	NED	0.0308	II-P	18, 19
2008in	NGC 4303	1566	NED	0.0192	II-P	20, 21
2009N	NGC 4487	1036	NED	0.0179	II-P	22, 21
2009bw	UGC 2890	1155	NED	0.1976	II-P	23[d]
2009js	NGC 918	1507	NED	0.3031	II-P	24
2009md	NGC 3389	1308	NED	0.0233	II-P	25, 26[d]
2012A	NGC 3239	753	NED	0.0274	II-P	27[d]
2012aw	NGC 3351	778	NED	0.0239	II-P	28, 29
2013ej	NGC 628	657	NED	0.0597	II-L	30, 31

Notes.
[a] Adopted heliocentric SN redshift.
[b] Source of SN redshift; NED: NASA/IPAC Extragalactic Database (http://ned.ipac.caltech.edu/); H01: Hamuy (2001); L02a: Leonard et al. (2002a); V06: Vinkó et al. (2006); here: this work.
[c] Galactic reddenings from Schlafly & Finkbeiner (2011).
[d] Expansion velocities measured in the reference.
References. (1) Calán/Tololo SN survey; (2) SOIRS; (3) Leonard et al. 2002a; (4) Leonard et al. 2002b; (5) Tsvetkov 2006; (6) Poznanski et al. 2009; (7) CATS; (8) Spiro et al. 2014; (9) Van Dyk et al. 2003; (10) Tsvetkov 2008; (11) Maguire et al. 2010; (12) Hendry et al. 2006; (13) Vinkó et al. 2006; (14) Tsvetkov et al. 2008; (15) Sahu et al. 2006; (16) Misra et al. 2007; (17) Tsvetkov et al. 2006; (18) Pastorello et al. 2006; (19) Pastorello et al. 2009; (20) Roy et al. 2011; (21) CSP; (22) Takáts et al. 2014; (23) Inserra et al. 2012; (24) Gandhi et al. 2013; (25) Fraser et al. 2011; (26) Bose & Kumar 2014; (27) Tomasella et al. 2013; (28) Bose et al. 2013; (29) Dall'Ora et al. 2014; (30) Richmond 2014; (31) C. Buil.

where $m_{\bar{\lambda}}$ is the apparent magnitude in a photometric band with central wavelength $\bar{\lambda}$ and band transmission function $S_{\bar{\lambda}}(\lambda)$, and

$$\widetilde{\mathcal{M}}_{\bar{\lambda},i}(A_G, z, A_h) \equiv -2.5 \log \int d\lambda S_{\bar{\lambda}}(\lambda) \mathcal{N}_{\lambda',i} 10^{-0.4(A_h(\lambda')+A_G(\lambda))} + \mathrm{ZP}_{\bar{\lambda}}. \quad (4)$$

$\mathrm{ZP}_{\bar{\lambda}}$ is the zero point of the magnitude scale, which is determined forcing the synthetic magnitude of a star with spectrophotometry $n_{\lambda}^{\mathrm{star}}$ to match its apparent magnitude $m_{\bar{\lambda}}^{\mathrm{star}}$, i.e.,

$$m_{\bar{\lambda}}^{\mathrm{star}} = -2.5 \log \int d\lambda S_{\bar{\lambda}}(\lambda) n_{\lambda}^{\mathrm{star}} + \mathrm{ZP}_{\bar{\lambda}}. \quad (5)$$

We can write Equation (3) as

$$\mathcal{M}_{\bar{\lambda},i} = m_{\bar{\lambda},i}^{\mathrm{corr}} - A_h(\bar{\lambda}) - 5 \log \left(\frac{D_L}{R'_{\mathrm{ph},i}} \right), \quad (6)$$

$$m_{\bar{\lambda},i}^{\mathrm{corr}} \equiv m_{\bar{\lambda},i} - A_G(\bar{\lambda}) - K_i(\bar{\lambda}), \quad (7)$$

where $\mathcal{M}_{\bar{\lambda},i} \equiv \widetilde{\mathcal{M}}_{\bar{\lambda},i}(A_G = z = A_h = 0)$, $A_G(\bar{\lambda})$ and $A_h(\bar{\lambda})$ are the Galactic and host galaxy broadband extinction, respectively, and

$$K_i(\bar{\lambda}) \equiv -2.5 \log(1+z) + 2.5 \log \left(\frac{\int d\lambda S_{\bar{\lambda}}(\lambda) \mathcal{N}_{\lambda,i} 10^{-0.4 A_h(\lambda)}}{\int d\lambda' S_{\bar{\lambda}}(\lambda) \mathcal{N}_{\lambda',i} 10^{-0.4 A_h(\lambda')}} \right) \quad (8)$$

is the K-term (see Schneider et al. 1983).

3.2. Photospheric Magnitude

We note that Equation (6) is similar to the definition of the distance modulus. $M_{\bar{\lambda}}$ is defined as the magnitude seen at 10 pc from the source. Similarly, Equation (6) relates the apparent magnitude to $\mathcal{M}_{\bar{\lambda}}$, a quantity not at 10 pc but just above the photosphere. We will call it photospheric magnitude. Absolute and photospheric magnitude are related by

$$\mathcal{M}_{\bar{\lambda},i} = M_{\bar{\lambda},i} - \mathcal{R}_i, \quad (9)$$

$$M_{\bar{\lambda},i} = m_{\bar{\lambda},i}^{\mathrm{corr}} - A_h(\bar{\lambda}) - \mu, \quad (10)$$

where μ is the distance modulus, and

$$\mathcal{R}_i \equiv 5 \log \left(\frac{10\,\mathrm{pc}}{R'_{\mathrm{ph},i}} \right). \quad (11)$$

3.3. Surface Brightness Method

The photospheric magnitude in Equation (6) can also be interpreted as an indicator of surface brightness, which on a magnitude scale is defined as

$$s_{\bar{\lambda}} = m_{\bar{\lambda}}^{\mathrm{corr}} + 5 \log \theta \quad (12)$$

(e.g., Wesselink 1969). The photosphere's angular size θ, used to calculate the area of the object in the sky, is also an indicator of R'_{ph}/D.

For Galactic cool giants, supergiants, and Cepheid variables, a relation is found between the surface brightness and a suitably chosen color index, which can be used as a proxy for temperature (Welch 1994; Fouqué & Gieren 1997; Kervella et al. 2004a). In the case of SNe II, atmosphere models show that the emergent flux, which depends on many parameters (e.g., chemical composition or density structure of the progenitor star), has an important dependence on temperature and, in short-wavelength bandpasses, density at the photosphere (Eastman et al. 1996). Thus we expect a relation between photospheric magnitude and a color index.

This kind of relation allows us to infer angular sizes using only photometric information and, comparing this with the physical size of the object estimated from the expansion, calculate distances. This method is known as the surface brightness method (SBM; Barnes & Evans 1976). In order to obtain distances with the SBM we need to measure the physical radius and calibrate the specific color–magnitude relation for SNe II.

3.3.1. Physical Radius

The gravitational binding energy of a SN II progenitor ($\sim 10^{49}$ erg) is much smaller than the expansion kinetic energy of the ejecta ($\sim 10^{51}$ erg), and the mass of the interstellar and circumstellar matter swept up by the SN in the first few months is also much smaller than the ejected mass, so any possible deceleration is negligible and therefore the envelope undergoes free expansion.

The physical radius of the photosphere under such conditions is given by

$$R_{\mathrm{ph}} = R(m_{\mathrm{ph}}, t) \approx v(m_{\mathrm{ph}})(t - t_0) + R_0(m_{\mathrm{ph}}), \quad (13)$$

where m_{ph} is the Lagrangian mass coordinate of the material instantaneously at the photosphere moving with velocity $v(m_{\mathrm{ph}})$ (hereafter, photospheric velocity, v_{ph}), t_0 is the shock breakout epoch, and $R_0(m_{\mathrm{ph}})$ is the radius of the SN at t_0. Due to the high expansion velocities ($\sim 10^4$ km s^{-1}), even for a large progenitor with $R_0 \sim 5 \times 10^{13}$ cm ($\sim 700\ R_{\odot}$), the initial radius is only $\sim 10\%$ of the photospheric radius at five days since shock breakout, so R_0 can be neglected after a few days. Then, we can estimate the radius of the photosphere for all but the first few days with the simple expression (distinguishing between the observer's frame and the SN restframe)

$$R'_{\mathrm{ph}} = v'_{\mathrm{ph}} \frac{t - t_0}{1+z}. \quad (14)$$

The photospheric velocity can be estimated from absorption minima of P Cygni profiles seen in a spectrum (Kirshner & Kwan 1974). Traditionally, weak lines (e.g., Fe II lines) are used for this purpose (e.g., Schmidt et al. 1992). This is based on the assumption that those lines are optically thin above the photosphere, being better indicators of the photospheric velocity than strong, optically thick lines (e.g., Balmer lines) formed well above the photosphere (Leonard et al. 2002a).

3.3.2. Calibration of the Photospheric Magnitude

Methods for measuring distances to SNe II based on atmosphere models, such as the expanding photosphere method (EPM; Kirshner & Kwan 1974; Schmidt et al. 1992), have a typical uncertainty of 15% in distance (Jones et al. 2009). Both the EPM and the SBM are based on Baade's (1926) method, so the uncertainty of an SBM distance will not be very different to the typical EPM uncertainty if we calibrate the color–photospheric magnitude relation with SN II atmosphere models.

In this work, however, we will obtain the photospheric magnitude calibration empirically. A calibration based on

Equation (12) is not possible because we cannot measure the SN angular size directly with the current optical instrumentation. Therefore, for the photospheric magnitude calibration, paying attention to Equation (6), we need SNe in galaxies with well-determined distances. Also, for calibration and distance measurements, we need precise knowledge of the SN shock breakout epoch and host galaxy extinction.

To measure expansion velocities and perform the K correction we need to know the SN redshift. For 25 SNe we estimate this quantity by measuring the peak wavelength of the narrow emission lines resulting from the superposed H II region (e.g., Leonard et al. 2002b). For the other 22 SNe the aforementioned emission line is not detected, so we adopt the redshift of the host galaxy nucleus, while for SN 1991al, SN 1999em, and SN 2004dj we adopt the values from Hamuy (2001), Leonard et al. (2002a), and Vinkó et al. (2006), respectively.

Schmidt et al. (1994) discussed that K corrections become significant for SNe at redshifts greater than 10^4 km s^{-1}. Thus, for the sake of simplicity, in the first step of testing the reliability of the photospheric magnitude, we use only SNe with $cz < 10^4$ km s^{-1} to avoid performing the K correction. However, we will keep the first term of the K-term (Equation (8)) to take into account the dispersion of up to ∼0.04 mag that introduces this term.

4. CRUCIAL PARAMETERS

4.1. Host Galaxy Extinction: The C3 Method

The host galaxy extinction can be estimated both from spectroscopic and photometric data. The main spectroscopic method is based on the comparison between an observed spectrum and SN II atmosphere model spectra, where the fitting parameters are the amount of reddening and the photospheric temperature (e.g., Dessart & Hillier 2006; Dessart et al. 2008). The main photometric method for SNe II-P assumes that, due to the H recombination nature of their photospheres, they should evolve from a hot initial stage to one of constant photospheric temperature, reaching the same color at a certain epoch (e.g., Olivares et al. 2010). In both cases, differences between an observed SN and models or other SNe consistent with zero reddening, are attributed to a color excess $E(C)$. The latter is associated with the host galaxy extinction $A(\bar{\lambda})$ by means of the extinction-to-reddening ratio,

$$R_{\bar{\lambda},C} = A(\bar{\lambda})/E(C), \tag{15}$$

where $R_{\bar{\lambda},C}$ can be derived from a Cardelli reddening law (hereafter CCM; Cardelli et al. 1989; O'Donnell 1994) as a function of $R_V \equiv A_V/E(B-V)$.

The main problem with estimating reddening using the aforementioned photometric method is selecting the time when SNe reach the same color (for which we also need to know the shock breakout epoch). To avoid these problems, we will use color instead of time to express the SN color evolution, i.e., we will use color–color curves (C3) to estimate reddening.

With data from the {$BVRI$} filter set, it is possible to define three independent color indices. In this work we choose to use $B-V$, $V-R$, and $V-I$. They are related to their intrinsic values (hereafter marked with zero subindex) through

$$\begin{aligned} B-V &= (B-V)_0 + E(B-V), \\ V-R &= (V-R)_0 + E(V-R), \\ V-I &= (V-I)_0 + E(V-I), \end{aligned} \tag{16}$$

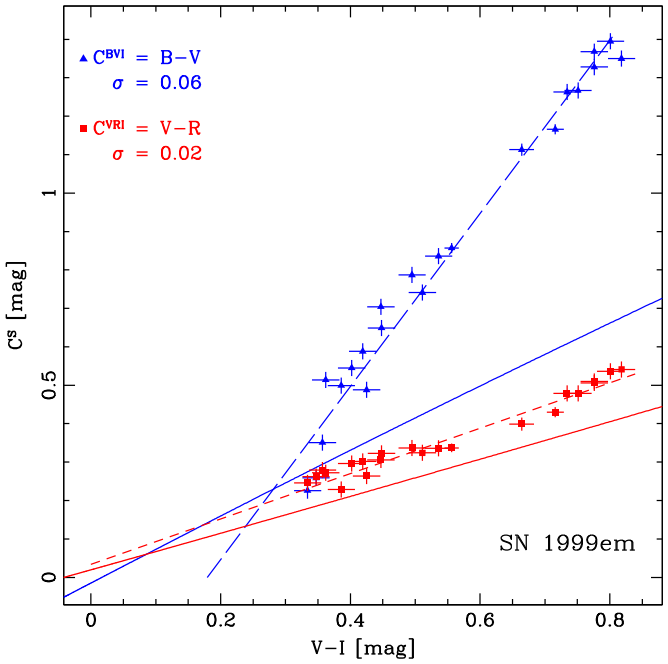

Figure 1. Color–color diagram showing the C3 of a blackbody (solid lines) and of SN 1999em (dashed lines) during the photospheric phase. Differences between them are due to the SN not being a perfect blackbody, to the presence of spectral lines, and also to the reddening that affects the SN. Line blanketing makes the difference stronger in the B band. The linear fit is more accurate for the VRI points ($\sigma = 0.02$) than for the BVI points ($\sigma = 0.06$).

where $E(\bar{\lambda}_1 - \bar{\lambda}_2) = A(\bar{\lambda}_1) - A(\bar{\lambda}_2)$ are the color excesses. For a blackbody there is an approximately linear relation between any two color indices because both of them are approximated functions of $1/T$. We expect that SNe II would hold a similar relation during their photospheric phase. There will be differences, though, because SNe II are not perfect blackbodies, have a spectral diversity, and are also affected by reddening. Figure 1 shows the $B-V$ versus $V-I$ and $V-R$ versus $V-I$ C3 for a blackbody (solid lines) and the data of SN 1999em in the photospheric phase (points). We see that the $V-R$ versus $V-I$ points have a linear behavior (short dashed line) meaning that the blackbody assumption is fairly good. The presence of spectral peculiarities causes differences between the observed and blackbody C3. This is more evident in the color index $B-V$ (long dashed line), where line blanketing generates a significant difference with a blackbody. Thus, for the case of an unreddened SN, we write the $V-R$ versus $V-I$ C3 as, approximately,

$$(V-R)_0 = n_0^{VRI} + m_0^{VRI}(V-I)_0. \tag{17}$$

For the $B-V$ versus $V-I$ C3 we write the same form, although it will be a less accurate approximation:

$$(B-V)_0 = n_0^{BVI} + m_0^{BVI}(V-I)_0. \tag{18}$$

If there is extinction, points from Equations (17) and (18) will be moved to the right in a color–color diagram (as Figure 1) by color excess $E(V-I)$ and upward by color excesses $E(V-R)$ and $E(B-V)$ respectively, i.e., they will be shifted in the color–color diagram by the reddening vectors

$$(E(V-I), E(V-R)) \equiv E_{VRI}, \tag{19}$$

$$(E(V-I), E(B-V)) \equiv E_{BVI}. \tag{20}$$

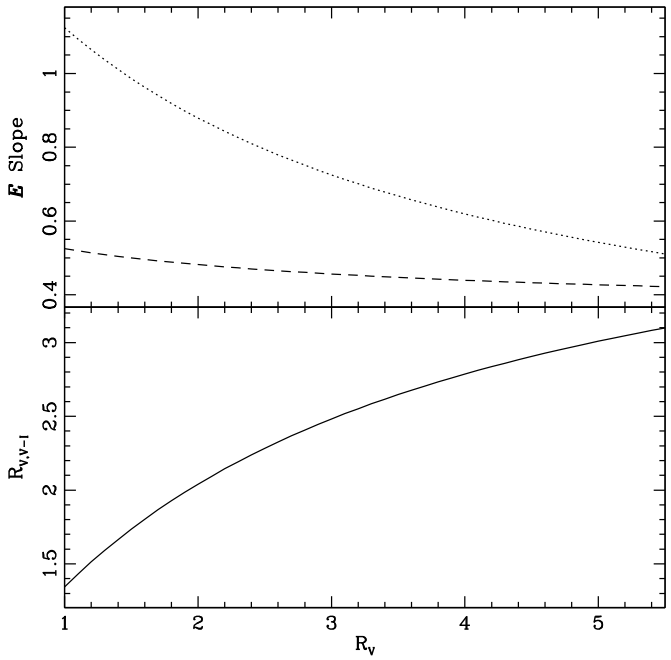

Figure 2. Dependence with R_V of m_E^{VRI}, m_E^{BVI} (top; dashed and dotted lines, respectively), and $R_{V,V-I} = A_V/E(V-I)$ (bottom). The curves are computed with SNe II spectra during the photospheric phase and with the CCM reddening law.

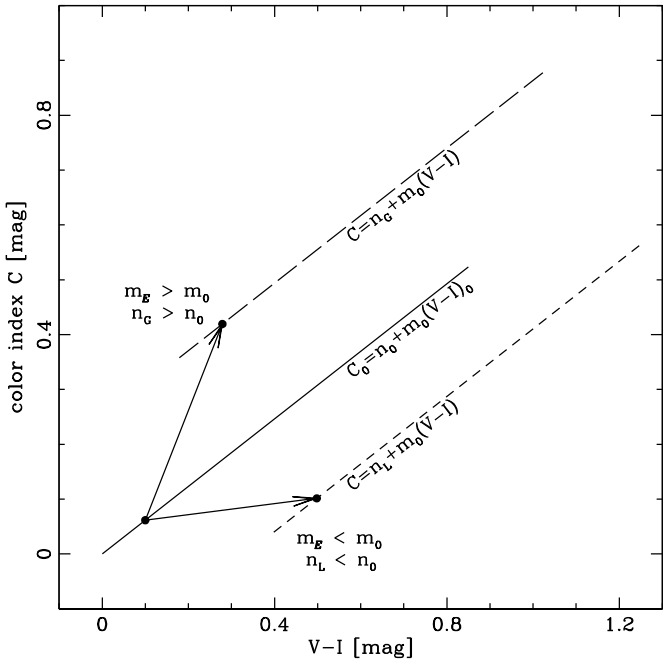

Figure 3. Example of the reddening effect on a linear C3. The unreddened C3 (solid line) is moved up if the slope of the reddening vector (m_E) is larger than the C3 slope (m_0), producing a reddened C3 (long dashed line) with a greater y-intercept (n_G). If $m_E < m_0$, then the unreddened C3 is moved down, producing a reddened C3 (short dashed line) with a lower y-intercept (n_L).

Since the color excesses are proportional to A_V, the lengths of E_{VRI} and E_{BVI} are proportional to the amount of extinction, and their slopes,

$$m_E^{VRI} \equiv \frac{E(V-R)}{E(V-I)} \tag{21}$$

and

$$m_E^{BVI} \equiv \frac{E(B-V)}{E(V-I)}, \tag{22}$$

are constants for a given R_V. Top of Figure 2 shows the dependence of m_E^{VRI} and m_E^{BVI} on R_V, both computed with SNe II spectra during the photospheric phase and the R_V parameterization of $A_{\bar{\lambda}}/A_V$ given by the CCM reddening law. Thus, the reddening vectors only modify the zero point of the C3 in the color–color diagram but not its slopes. So, the C3 for the SN affected by reddening can be expressed as

$$V-R = n^{VRI} + m_0^{VRI}(V-I), \tag{23}$$

$$B-V = n^{BVI} + m_0^{BVI}(V-I). \tag{24}$$

Figure 3 shows the effect of the reddening vector over an unreddened C3. The C3 is moved above or below the unreddened C3 depending on whether the slope of the reddening vector is larger or smaller than the slope of the C3.

In general, with $BVRI$ photometric data, we can determine color excesses with the $\{VRI\}$ filter subset (Equation (23) minus Equation (17)) or with the $\{BVI\}$ filter subset (Equation (24) minus Equation (18)), and the corresponding uncertainty via

$$E_S(V-I) = \frac{n^S - n_0^S}{m_E^S(R_V) - m_0^S}, \tag{25}$$

$$\sigma_{E_S(V-I)} = \frac{\sqrt{\sigma_{n^S}^2 + \sigma_{n_0^S}^2 + \sigma_{m_0^S}^2 E_S(V-I)^2}}{\left|m_E^S(R_V) - m_0^S\right|}, \tag{26}$$

where $S = \{VRI\}, \{BVI\}$. We see that the applicability of the method through Equation (25) depends strongly on the value of $|m_E^S(R_V) - m_0^S|$: if the value is small, then the reddening vector moves points along the C3 and no reliable reddening determination is possible. The visual extinction is obtained through the extinction-to-reddening ratio (see bottom of Figure 2):

$$R_{V,V-I}(R_V) = \frac{A_V}{E(V-I)}. \tag{27}$$

We note that the method presented above is essentially the same method proposed by Natali et al. (1994) to measure reddening for open clusters, which shows a linear relation between $B-I$ and $B-V$ color indices (for further discussion of the method, see Munari & Carraro 1996). Hereafter we will refer to this method simply as the C3 method.

In order to compute color excesses with Equation (25), we need to determine for each SN the unreddened C3 parameters n_0^S and m_0^S and the value of R_V. This task can be carried out in a simple way with the following two assumptions:

1. *SNe II have a similar spectral evolution during the photospheric phase*. This is partly supported by results of SN II atmosphere models, which show that the emergent flux depends mainly on temperature (Eastman et al. 1996; Jones et al. 2009). In that case, SNe II should have approximately the same intrinsic C3 with slope m_0^S. As the C3 slope is not affected by reddening, the value of m_0^S does not depend on dust extinction or dust properties (i.e., reddening law and R_V). However, there could be intrinsic differences due to the variations on the SN parameters, mainly those involved with the line profile formation (e.g., metallicity, density, and expansion velocity profile).
2. *All dust in SNe II sightlines is described by the same R_V*. SNe II tend to appear near H II regions, so the value of R_V to use should be representative for these regions. In

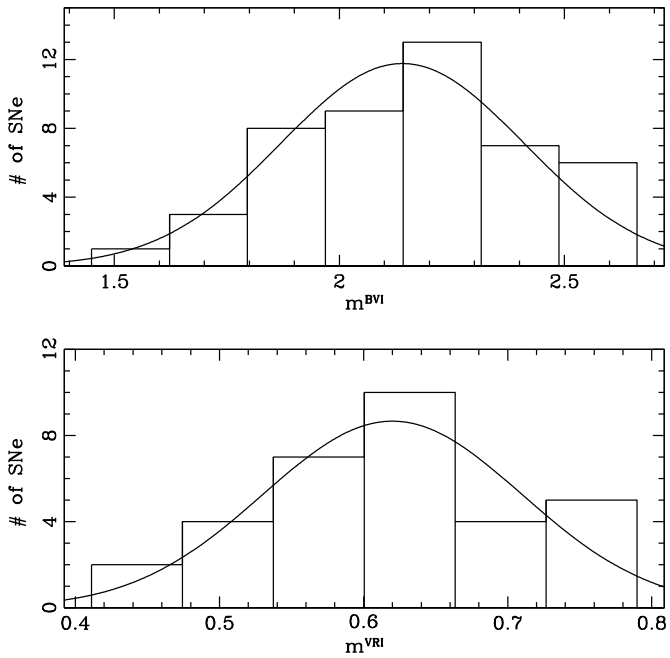

Figure 4. C3 slope distribution for SNe for the $\{BVI\}$ (top) and $\{VRI\}$ (bottom) filter subsets, where the solid line is the Gaussian distribution computed with the respective values for the mean and standard deviation.

that case, the slope of reddening vectors will be the same for all SNe. This allows us to identify the SN with the smallest reddening in a given SN set (see Figure 3): that with the lowest value of n^s if the slope of the reddening vector is larger than m_0^s, or that with the highest value of n^s if the slope of the reddening vector is lower than m_0^s. If the SN found with the smallest reddening with this method is consistent with the small reddening found with other methods, then we can set its y-intercept as n_0^s.

4.2. Shock Breakout Epoch

The shock breakout epoch t_0 is one of the most important parameters in determining the actual stage of the expanding photosphere. This value is estimated as lying between the last nondetection t_n and the first detection t_f of the SN, where the first detection can be the discovery epoch t_d or the time of a prediscovery detection if it is available. Defining t_m as the midpoint between t_n and t_f, and the uncertainty Δt as half the time between t_n and t_f, i.e.,

$$t_m = (t_n + t_f)/2 - t_d, \tag{28}$$

$$\Delta t = (t_f - t_n)/2 \tag{29}$$

(where we choose to express time with respect to t_d), we can locate the shock breakout epoch in the range $t_m - \Delta t < t_0 < t_m + \Delta t$ (e.g., D'Andrea et al. 2010). We use Δ instead of σ to emphasize that the uncertainty is not Gaussian but uniform, with a probability distribution described by a top hat function.

If an SN has a t_n that yields a very high Δt, or there is simply no nondetection report for the SN, then we use the shock breakout epoch obtained through the Supernova Identification code (Blondin & Tonry 2007) given in Anderson et al. (2014). For some SNe we compare their earliest spectra with a library of SN spectra using the GELATO[7] tool (Harutyunyan et al. 2008), then we constrain t_0 between the lowest and the highest value of t_0 estimated with the spectra comparison.

Table 2 lists the midpoint epochs and the uncertainties (Column 7) for our SN set, with the respective references (Column 8).

5. ANALYSIS

5.1. Application of the C3 Method

Table 2 lists the C3 slope values obtained for the SNe in the $\{VRI\}$ (Column 2) and $\{BVI\}$ (Column 3) filter subsets. SN 2003gd and SN 2003ho do not describe clear straight lines in the color–color diagram because for these SNe we have only late-time photometry, so we discard them for the C3 intrinsic slope determination. We also rule out SN 1991al and SN 2002ew due to poor sampling in the B and I bands, respectively. We obtain mean slopes of $\langle m^{BVI} \rangle = 2.14$ and $\langle m^{VRI} \rangle = 0.62$ with standard deviations of 0.27 and 0.09, respectively. In each filter subset the measurement errors for the C3 slopes are lower than the standard deviation, so this value represents the intrinsic diversity in the C3 slope value. Therefore we adopt $m_0^{BVI} = 2.14 \pm 0.27$ and $m_0^{VRI} = 0.62 \pm 0.09$. Figure 4 shows the distribution of C3 slopes.

The next step is to compare the value of the intrinsic C3 slope with the respective reddening vector slopes. For $R_V \geqslant 1$, $|m_E^{VRI} - m_0^{VRI}| \leqslant 0.2$ (see top of Figure 2). This means that in the case of a $C3_{VRI}$ the displacement produced by reddening is virtually along the locus given by the same C3, so the C3 method for the $\{VRI\}$ filter subset is not suitable for measuring reddening. For the $\{BVI\}$ filter subset $|m_E^{BVI} - m_0^{BVI}| > 1$, so the C3 method for this filter subset (hereafter $C3(BVI)$) is very promising for measuring reddening.

To obtain the values of n^{BVI} for each SN, we first correct photometry for reddening due to our Galaxy using a Fitzpatrick (1999) reddening law and $R_V = 3.1$ (Schlafly & Finkbeiner 2011). Then we adjust a straight line keeping the slope m_0^{BVI} in the linear fitting. In order to include the uncertainty of m_0^{BVI} in the n^{BVI} uncertainty, we perform Monte Carlo simulations varying randomly the slope according to its uncertainty. Table 2 lists the C3 y-intercept values for the SNe in the $\{BVI\}$ filter subset (Column 4). In order to set the zero point for the color excesses, we need to choose those SNe with the smallest reddening according to the criterion given in Section 4.1, i.e., those with the lowest value of n if the slope of the reddening vector is larger than the C3 slope, or those with the highest value of n if the slope of the reddening vector is smaller than the C3 slope. Using the top panel of Figure 2 we can confirm that m_E^{BVI} is smaller than m_0^{BVI} for $R_V \geqslant 1$ with a high confidence level ($m_E^{BVI} < m_0^{BVI} - 3\sigma_{m_0^{BVI}}$). In other words, for all the reasonable values of R_V, the reddening vector moves the C3 to the lower right corner of Figure 3, and therefore the SN with the highest value of n^{BVI} corresponds to the SN with the smallest reddening. Among our SNe, SN 1992af and SN 2008in have the highest values of n^{BVI}. SN 2008in spectra show Na I D absorption features at the redshift of the host galaxy, indicating a small reddening of $A_V = 0.08$ mag (Anderson et al. 2014), while for SN 1992af, for which we did not detect Na I D lines, Olivares et al. (2010) found a high amount of reddening through spectroscopic analysis (see Column 5 of Table 2). To determine if SN 1992af and SN 2008in can be use as a reddening zero point, we will analyze a group of four SNe with high and nearly equal values of n^{BVI}, namely, SN 1993S, SN 1999eg, SN 2003bn, and SN 2013ej.

[7] https://gelato.tng.iac.es

Table 2
SN II Parameters

SN Name	$m^{VRI}(\sigma)$	$m^{BVI}(\sigma)$	$n^{BVI}(\sigma)$[a] (mag)	A_V(spec)(σ)[b] (mag)	$A_V(BVI)(\sigma)$ (mag)	$t_m(\Delta t)$[c] (days)	References[d]
1991al	0.67(0.02)	3.64(0.06)	−0.57(0.07)	0.33(0.16)	0.61(0.17)	−15.2(9.0)[e]	I 5310, A14
1992af	···	2.05(0.04)	−0.14(0.07)	1.26(0.31)	−0.15(0.13)	−12.3(6.0)[e]	I 5554, A14
1992ba	···	2.18(0.02)	−0.32(0.05)	0.46(0.16)	0.16(0.10)	−6.5(6.5)	I 5625, 5632
1993A	···	2.27(0.03)	−0.29(0.04)	0.08(0.31)	0.10(0.09)	−9.6(9.6)	I 5693
1993S	···	2.47(0.04)	−0.23(0.05)	···	0.00(0.10)	−4.4(4.0)[e]	I 5812, A14
1999br	0.49(0.01)	2.01(0.02)	−0.58(0.04)	0.26(0.16)	0.62(0.14)	−4.0(4.0)	I 7141, 7143
1999ca	0.73(0.01)	2.52(0.02)	−0.31(0.05)	0.17(0.31)	0.15(0.10)	−19.6(7.0)[e]	I 7158, A14
1999cr	0.76(0.01)	2.35(0.02)	−0.55(0.04)	0.51(0.31)	0.57(0.13)	−3.2(7.0)[e]	I 7210, A14
1999eg	0.71(0.02)	2.56(0.04)	−0.22(0.04)	···	−0.01(0.07)	−2.1(2.1)[e]	I 7275, H08
1999em	0.60(0.01)	2.24(0.02)	−0.28(0.03)	0.33(0.16)	0.09(0.06)	−4.5(4.5)	I 7294
1999gi	0.57(0.01)	2.24(0.03)	−0.79(0.05)	0.57(0.16)	0.99(0.21)	−3.3(3.3)	I 7329, 7334
2001X	0.62(0.03)	2.34(0.11)	−0.38(0.06)	···	0.27(0.12)	−5.2(5.2)	I 7591
2002ew	···	···	−0.53(0.10)	···	0.54(0.20)	−10.2(10.2)	I 7964
2002gd	···	2.28(0.02)	−0.49(0.05)	···	0.46(0.13)	−0.6(0.0)	I 7986, 7990
2002gw	···	2.45(0.03)	−0.57(0.05)	0.41(0.19)	0.61(0.14)	−2.3(5.0)[e]	I 7995, A14
2002hj	···	2.31(0.04)	−0.34(0.07)	0.21(0.31)	0.21(0.13)	−5.7(5.7)	I 8006
2002hx	···	1.45(0.02)	−0.48(0.09)	0.18(0.25)	0.46(0.18)	−8.0(8.0)	I 8015
2003B	0.56(0.01)	2.66(0.03)	−0.29(0.05)	0.01(0.25)	0.12(0.10)	−29.5(11.0)[e]	I 8042, A14
2003E	···	2.31(0.02)	−0.74(0.08)	1.11(0.31)	0.91(0.22)	−11.3(7.0)[e]	I 8044, A14
2003T	···	2.21(0.03)	−0.44(0.06)	0.54(0.31)	0.38(0.14)	−10.0(10.0)	I 8058
2003Z	0.62(0.02)	2.01(0.04)	−0.41(0.07)	···	0.32(0.15)	−4.5(4.5)	I 8062
2003bl	···	1.99(0.04)	−0.36(0.09)	0.01(0.16)	0.24(0.17)	−2.5(3.0)[e]	I 8086, A14
2003bn	···	2.37(0.03)	−0.22(0.04)	0.12(0.16)	−0.01(0.08)	−6.1(0.7)	I 8088
2003ci	···	1.98(0.04)	−0.31(0.09)	0.46(0.31)	0.14(0.16)	−8.0(8.0)	I 8097
2003cn	···	1.85(0.03)	−0.34(0.05)	0.01(0.25)	0.19(0.11)	−11.0(11.0)	I 8101
2003ef	···	1.79(0.02)	−0.68(0.10)	1.26(0.25)	0.79(0.23)	−21.0(0.0)	I 8131, 8132
2003ej	···	2.03(0.04)	−0.53(0.08)	···	0.54(0.17)	−4.5(4.5)	I 8134
2003fb	0.77(0.01)	1.95(0.03)	−1.04(0.14)	0.45(0.31)	1.44(0.36)	−20.5(6.0)[e]	I 8143, A14
2003gd	0.99(0.02)	1.11(0.02)	−0.48(0.09)	0.43(0.31)	0.45(0.19)	−50.0(30.2)[e]	I 8150, H08
2003hg	0.63(0.06)	2.47(0.01)	−1.07(0.09)	···	1.49(0.33)	−4.5(4.5)	I 8184
2003hk	0.71(0.01)	1.85(0.03)	−0.42(0.09)	0.67(0.31)	0.34(0.17)	−5.1(4.0)[e]	I 8184, A14
2003hl	0.66(0.01)	1.92(0.01)	−0.79(0.09)	1.27(0.25)	1.00(0.24)	−4.5(4.5)	I 8184
2003hn	0.66(0.01)	2.19(0.02)	−0.58(0.06)	0.60(0.25)	0.62(0.16)	−10.3(10.3)	I 8186
2003ho	0.86(0.01)	1.02(0.02)	−1.68(0.19)	1.26(0.31)	2.57(0.59)	−10.9(10.9)	I 8186
2003ib	0.60(0.02)	1.70(0.03)	−0.67(0.08)	···	0.78(0.20)	−10.0(5.0)	I 8201
2003ip	0.79(0.01)	1.82(0.02)	−0.43(0.08)	0.43(0.31)	0.37(0.17)	−18.3(4.0)[e]	I 8214, A14
2003iq	0.57(0.01)	2.21(0.03)	−0.39(0.08)	0.40(0.16)	0.29(0.16)	−1.5(1.5)	I 8219
2004A	0.41(0.02)	2.60(0.04)	−0.48(0.07)	···	0.45(0.16)	−6.9(6.9)	I 8265
2004dj	0.51(0.01)	2.33(0.03)	−0.43(0.05)	0.52(0.25)	0.36(0.12)	−20.4(17.4)[e]	I 8377, H08
2004et	0.61(0.01)	2.05(0.01)	−0.37(0.03)	0.15(0.25)	0.25(0.08)	−4.5(0.5)	I 8413
2005ay	0.50(0.05)	1.97(0.12)	−0.28(0.06)	···	0.10(0.11)	−3.7(3.7)	I 8500, 8502
2005cs	0.67(0.01)	1.99(0.01)	−0.37(0.03)	0.14(0.16)[f]	0.25(0.07)	−1.5(0.5)	I 8553, P09
2008in	0.49(0.01)	2.22(0.02)	−0.12(0.04)	···	−0.19(0.09)	−2.6(0.2)	C 1636, R11
2009N	0.57(0.01)	2.16(0.02)	−0.67(0.05)	···	0.79(0.17)	−10.9(10.9)	C 1670
2009bw	0.61(0.01)	2.50(0.02)	−0.50(0.04)	···	0.47(0.12)	−2.4(2.4)	C 1743, I12
2009js	0.47(0.02)	2.23(0.05)	−0.38(0.05)	···	0.27(0.11)	−5.5(5.5)	C 1969
2009md	0.65(0.03)	1.63(0.07)	−0.54(0.06)	···	0.55(0.15)	−7.9(7.9)	C 2065, F11
2012A	0.64(0.01)	1.93(0.02)	−0.40(0.03)	···	0.30(0.08)	−4.7(4.7)	C 2974
2012aw	0.59(0.01)	1.91(0.02)	−0.37(0.04)	···	0.26(0.09)	−0.8(0.8)	C 3054, A 3996
2013ej	0.63(0.01)	1.93(0.03)	−0.23(0.03)	···	0.01(0.06)	−1.6(0.3)	C 3606, A 5237

Notes. Column 1: SN names. Columns 2 and 3: C3 slopes in the $\{VRI\}$ and $\{BVI\}$ filter subsets, respectively. Column 4: C3 y-intercept for the $\{BVI\}$ filter subset. Columns 5 and 6: reddenings from spectroscopic analysis and from the C3(BVI) method respectively. Columns 7 and 8: midpoint epoch and references, respectively.

[a] Using a fixed slope $m_0^{BVI} = 2.14 \pm 0.27$.

[b] Reddenings from Olivares et al. (2010), unless otherwise noted, adapted to the calibration of Schlafly & Finkbeiner (2011) and assuming $R_V = 3.1$.

[c] Epochs are expressed with respect to the discovery time. The shock breakout epoch lies in the range $t_m - \Delta t < t_0 < t_m + \Delta t$.

[d] I: IAU Circular; C: IAU's Central Bureau for Astronomical Telegram; A: Astronomer's Telegram; H08: Harutyunyan et al. 2008; P09: Pastorello et al. 2009; F11: Fraser et al. 2011; R11: Roy et al. 2011; I12: Inserra et al. 2012; A14: Anderson et al. 2014.

[e] Unhelpful t_n.

[f] Dessart et al. (2008).

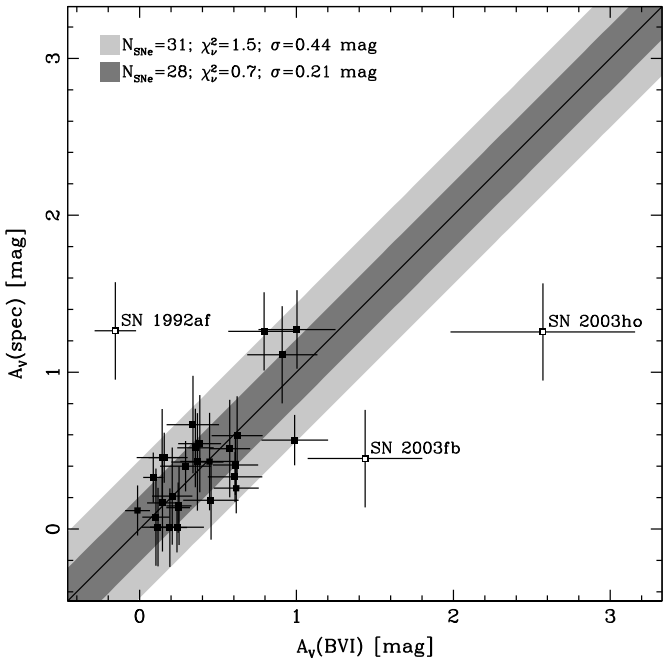

Figure 5. Comparison of A_V obtained with the spectrum-fitting method and those obtained with the C3(BVI) method. Solid line represents the one-to-one relation. Open squares correspond to the outliers of the correlation. The shaded regions contain data within 1σ of the perfect correlation: using all SNe in our SN set (light gray region) and discarding the outliers (dark gray region).

Among the four SNe found with possible small reddening levels, for SN 1993S and 2003bn we found no significant Na I D interstellar lines in their spectra at the redshifts of their host galaxies. A similar result was found by Valenti et al. (2014) for SN 2013ej. Thus these three SNe could be useful for defining the zero point for reddening. In the case of SN 1999eg, the available spectra are fairly noisy, so we cannot identify or discard the presence of Na I D lines. Therefore we do not use this SN to define the zero point for reddening. For the following analysis we adopt $n_0^{BVI} = -0.23 \pm 0.02$ mag, i.e., the weighted mean of the n^{BVI} values for SN 1993S, SN 2003bn, and SN 2013ej.

Table 2 summarizes previous reddening results obtained by Olivares et al. (2010) from spectroscopic analysis A_V(spec) (Column 5, adapted to the calibration of Schlafly & Finkbeiner 2011) and our C3(BVI) reddening results $A_V(BVI)$ (Column 6) for the SN set used in this work using a CCM reddening law with $R_V = 3.1$.

Figure 5 shows the comparison between reddenings from spectroscopic analysis and from the C3(BVI) method. We see that both methods are well correlated with the exception of SN 1992af, SN 2003fb, and SN 2003ho (empty squares), which increase the dispersion up to 0.44 mag. Our reddening measurement for SN 1992af, although negative, is consistent with zero reddening within 1.2σ. Considering the non-detection of Na I D lines, SN 1992af is more like a low-reddened than a high-reddened SN, as is suggested by spectroscopic analysis. When we include this SN in the group to define the reddening zero point, the value of n_0^{BVI} virtually does not change. For SN 2003ho we measure a Na I D equivalent width (EW) of 1.5 Å. Using the Poznanski et al. (2012) relation and assuming $R_V = 3.1$, the EW indicates $A_V \approx 2.5$ mag, consistent with our reddening estimation. In general, differences between photometric and spectroscopic results for these three SNe can also be due to the use of late-time spectra (with flux correction in the case of SN 1992af and SN 2003fb), which are not the best for reddening determination with the spectroscopic analysis (Olivares et al. 2010). Discarding the outliers, the dispersion is reduced to 0.21 mag, where the value of $\chi^2_\nu = 0.7$ indicates that the dispersion is slightly lower than the combined uncertainties of both techniques.

These results indicate that the C3(BVI) method can be used as a good reddening estimator, with SN 1992af, SN 1993S, SN 2003bn, and SN 2013ej as the reddening zero point, so we will use this method throughout this work. Although negative reddening values have no physical meaning, negative values in our SN set are statistically consistent with zero reddening, with the exception of SN 2008in which differs by 2.1σ from zero reddening. A possible explanation for the negative value is the effect of a high metallicity, which reduces the flux in the B band (via line blanketing) producing higher values of the $B-V$ color index. This effect moves the C3 upward, acting contrary to the reddening effect. Based on the correlation between metallicity and the strength of the Fe II 5018 Å absorption line displayed by theoretical models, Dessart et al. (2014) derive a metallicity for SN 2008in of $\approx 2\,Z_\odot$, which is the highest value in their SN set.[8] Thus it is possible that SN 2008in could be a low or zero reddened SN, with $n^{BVI} > n_0^{BVI}$ due to a high metallicity. Moreover, Dessart et al. (2014) find that SN 2003bn, one of our SNe used to set the reddening zero point, is among the SNe with the lowest metallicities in their SN set. Thus SN 2003bn, which is consistent with zero reddening, also works as a zero point for the metallicity effect. As the n^{BVI} value of SN 2003bn is virtually equal to n_0^{BVI}, we will keep this value as the reddening zero point, but we will set $A_V = 0$ mag for SN 2008in.

5.2. Photospheric Magnitude for SNe II

Since we are trying to understand the intrinsic dispersion of the color-based standardization, we do not want to introduce a large dispersion from the distances in our trial SN sample, so, in this work, we calibrate the photospheric magnitude using SNe with host galaxy distances measured with Cepheids. Among SNe with a shock breakout epoch uncertainty of a few days, we found four SNe, namely SN 1999em, SN 1999gi, SN 2005ay, and SN 2012aw, with Cepheid distances. For the host galaxy of SN 2005ay (NGC 3938) we adopt the Cepheid distance for NGC 3982 which, like NGC 3938, is a member of the Ursa Major Group. In the case of SN 1999gi, the distance of its host galaxy (NGC 3184) is estimated through Cepheid distances for NGC 3319 and NGC 3198, which Tully (1988) cataloged in a small group of four galaxies, although NGC 3184 is a relatively isolated galaxy (Leonard et al. 2002b). Table 3 shows the name and distance modulus of the host galaxy of the four aforementioned SNe II. We call this set "nearby SNe."

With the knowledge of the crucial parameters for our nearby SNe (Tables 2 and 3), we construct the photospheric magnitude according to Equation (9). For this, we need photometric and spectroscopic data at the same epoch. We choose to interpolate photometric points rather than spectroscopic data because in our SN set the former is better sampled. In order to do the photometric interpolation, we first realize fits to the light curves using the *Local Polynomial Regression Fitting* (Cleveland et al. 1992) which performs a polynomial regression over small local intervals along the domain using a routine called `loess`. We

[8] Roy et al. (2011), however, infer a sub-solar metallicity for the region of the SN occurrence.

Table 3
Host Galaxy Distance Moduli of the Nearby SNe

SN Name	Host Galaxy	$\mu(\sigma)$ (mag)
1999em	NGC 1637	30.40(0.07)
1999gi	NGC 3184	30.74(0.08)[a]
		30.80(0.08)[b]
2005ay	NGC 3938	31.87(0.15)[c]
2012aw	NGC 3351	30.10(0.07)

Notes. Values from Saha et al. (2006).
[a] From the Cepheid distance for NGC 3319, a possible member of a small group of four galaxies, which contains to NGC 3184 (Tully 1988).
[b] From the Cepheid distance for NGC 3198. Similar to the case of NGC 3319.
[c] From the Cepheid distance for NGC 3982, a member of the Ursa Major Group.

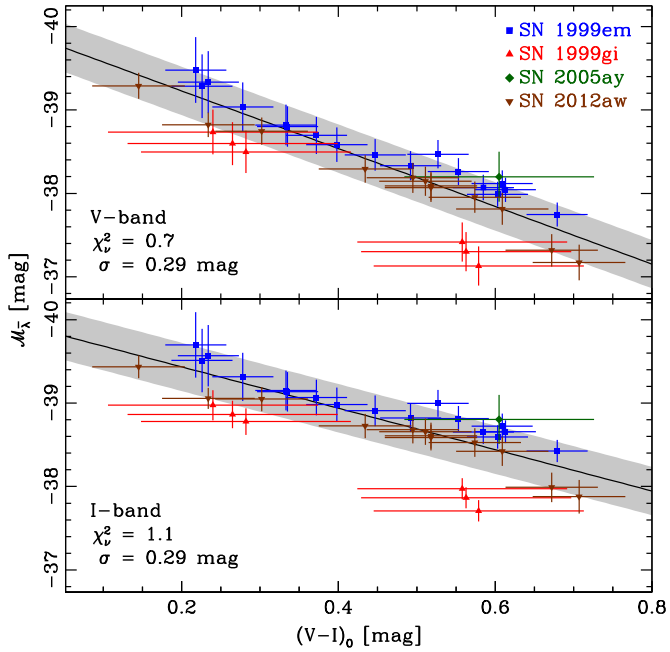

Figure 6. Photospheric magnitude vs. corrected $V-I$ color for our nearby SNe using V (top) and I (bottom) bands. The gray shading corresponds to the 1σ dispersion.

interpolate with cubic-spline, using the routine `splint` (Press et al. 1992).

For SNe II-P Poznanski et al. (2009) and Olivares et al. (2010) found values of $R_V = 1.5 \pm 0.5$ and $R_V = 1.4 \pm 0.1$, respectively, which are lower than the standard Galactic value of 3.1. Hereafter we will adopt $R_V = 1.5$ as the representative value for SNe II.

5.2.1. Color–Magnitude Diagram

Figure 6 shows the evolution of $\mathcal{M}_V$ (top) and $\mathcal{M}_I$ (bottom) with $V-I$ color for our nearby SNe throughout their photospheric phase.

The sequences are best represented by straight lines, i.e.,

$$\mathcal{M}_{\bar{\lambda}} = a_1 + a_2(V-I)_0. \tag{30}$$

The parameters of the linear fit are listed in Table 4. The values of $\chi^2_\nu \lesssim 1$ indicate that the intrinsic dispersion is undetectable at the current level of precision. Ignoring the observational uncertainties, the dispersion of 0.29 mag represents a relative distance scatter of 13%.

Table 4
Parameters for Photospheric Magnitude Fit

Adjust	$a_1(\sigma)$ (mag)	$a_2(\sigma)$[a]	$a_3(\sigma)$ (mag)	σ (mag)
$\mathcal{M}_V(V-I)$	−39.92(0.15)	3.46(0.30)	···	0.29
$\mathcal{M}_I(V-I)$	−39.92(0.15)	2.46(0.32)	···	0.29
$\mathcal{M}^*_V(t-t_0)$	−37.70(0.21)	0.55(0.26)	−2.85(0.23)	0.08
$\mathcal{M}^*_I(t-t_0)$	−38.99(0.27)	1.21(0.31)	−4.20(0.34)	0.09

Note. [a] Without units for color evolution and with units of mag for time evolution.

5.2.2. Photospheric Light Curve

For each SN II the photospheric magnitude is a time-dependent quantity, which is given implicitly in Equation (9) by the i subindex. In that case, points describe a light curve where, in addition to being corrected by distance, as in the case of an absolute light curve, they are also corrected by the $\mathcal{R}$-term. We can see in Figure 6 that time enters as an independent variable on both axes: in the case of $\mathcal{M}_{\bar{\lambda},i}$ through the $\mathcal{R}$-term (this is an inference from theory) and in the case of the $(V-I)_0$ color, from its evolution with time (this is an empirical inference). We then remove the factor $t - t_0$ included in the $\mathcal{R}$-term, i.e.,

$$\mathcal{M}_{\bar{\lambda},i} - 5\log\left(\frac{t-t_0}{100\ \text{days}}\right) = m^{\text{corr}}_{\bar{\lambda},i} - A_h(\bar{\lambda}) - \mu - \mathcal{R}^*_i \equiv \mathcal{M}^*_{\bar{\lambda},i}, \tag{31}$$

where now

$$\mathcal{R}^*_i \equiv 5\log\left(\frac{10\ \text{pc}/100\ \text{days}}{v_{\text{ph},i}}\right) \tag{32}$$

gives the correction by the size of the source where time is given implicitly in the i subindex. As we remove time from the y-axis, the uncertainty in this axis is reduced and becomes uncorrelated with the uncertainty of the new x-axis.

Figure 7 shows the time evolution of $\mathcal{M}^*_V$ (top) and $\mathcal{M}^*_I$ (bottom) for our nearby SNe throughout their photospheric phase, with the shock breakout epoch as the time reference. Modeling $m^{\text{corr}}_{\bar{\lambda}}$ during the photospheric phase as a straight line and the photospheric velocity as a power law, i.e.,

$$v_{\text{ph}} = \alpha\left(\frac{t-t_0}{100\ \text{days}}\right)^{\beta} \tag{33}$$

(e.g., Olivares et al. 2010), the function to fit will be

$$\mathcal{M}^*_{\bar{\lambda}} = a_1 + a_2\left(\frac{t-t_0}{100\ \text{days}}\right) + a_3\log\left(\frac{t-t_0}{100\ \text{days}}\right). \tag{34}$$

The parameters of the fit are listed in Table 4. The mean dispersion of 0.09 mag implies relative distances with a precision of 4%.

We see that, by replacing color with time, the dispersion is reduced. It is not an expected result because temperature (estimated through a color index) should be a variable more correlated with the SN flux than time. Switching the independent axis from color to time involves bringing in the relation between color and time, i.e., the color curve. However, even if our nearby SNe have the same color curve, points from Figure 6

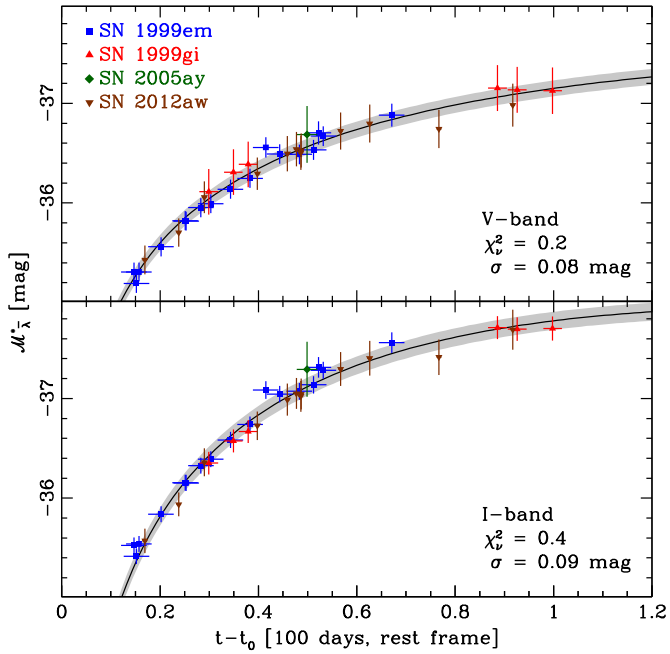

Figure 7. $\mathcal{M}^*_V$ and $\mathcal{M}^*_I$ evolution with time since shock breakout epoch for our nearby SNe, using V (top) and I (bottom) bands. The gray shading corresponds to the 1σ dispersion.

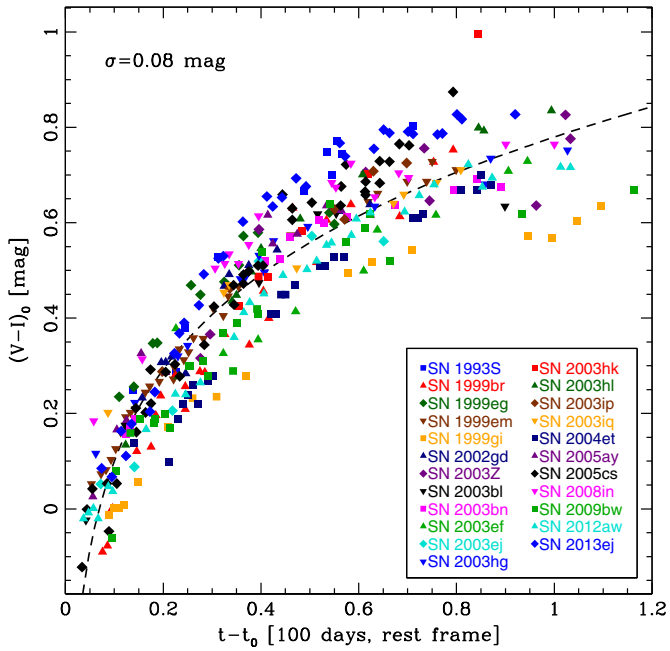

Figure 8. $V-I$ color curves in the restframe of 23 SNe II during the photospheric phase with a shock breakout epoch uncertainty smaller than 4.5 days (the uncertainty for SN 1999em), corrected for Galactic and host galaxy extinction. The scatter of 0.08 mag with respect to the average color curve (dashed line) indicates that the assumption of a same color curve for SNe II would be inaccurate.

would be moved in the x-axis in the same way, and therefore would show the same scatter as in Figure 7. Suppose that the good behavior of photospheric magnitude with time is a general result with a characteristic dispersion of 0.09 mag. Figure 8 shows the $V-I$ color curves of 23 SNe in our set with a shock breakout epoch uncertainty lower than 4.5 days (the uncertainty for SN 1999em), corrected by Galactic and host galaxy extinction. The scatter in the branch is principally due to differences between the color curves of each SNe, so we can estimate an average color curve with a scatter of 0.08 mag. Replacing time with color in Figure 7, the scatter in color produces an indirect contribution of ∼0.24 mag to the y-axis, producing a total dispersion of ∼0.26 mag or 12% in relative distances. This result is consistent with the dispersion obtained using our nearby SNe (Figure 6) and with the typical scatter of 15% in relative distances obtained with SN atmosphere models through the EPM (Jones et al. 2009).

The small scatter found for the photospheric light curve, although it was obtained with four SNe only, gives us a hint about a possible homogeneity degree in the radiative process of SNe II during the photospheric phase. This conclusion could be debated considering the diversity of slopes and magnitudes of SN II light curves (e.g., Figure 2 in Anderson et al. 2014). Here the $\mathcal{R}$-term correction becomes crucial.

Similar to Equation (9),

$$M_{\bar{\lambda},i} = \mathcal{M}^*_{\bar{\lambda},i} + \mathcal{R}^*(v_{\mathrm{ph},i}), \tag{35}$$

where the photospheric magnitude and the $\mathcal{R}$-term are given by Equations (31) and (32), respectively. Equation (35) reads: if the photospheric magnitude evolution is the same for all SNe II, then the shape of the light curve is defined mostly by the evolution of the $\mathcal{R}$-term, which in turn depends on the velocity evolution. With Equation (35) we can understand the diversity of the observed SN II light curves during the photospheric phase in terms of the diversity of velocity evolution:

1. The slope of the light curve is given by

$$\dot{M}_{\bar{\lambda},i} = \dot{\mathcal{M}}^*_{\bar{\lambda},i} + \frac{5}{\ln(10)}\frac{|\dot{v}_{\mathrm{ph},i}|}{v_{\mathrm{ph},i}}, \tag{36}$$

   where dots denote temporal derivative. For example, SNe with less massive H envelopes (i.e., photospheres not being well supported by the H recombination) have photospheres receding rapidly in mass coordinate, therefore, from Equation (36) they have steeper light curves than H-rich SNe. The previous description is the usual one used to distinguish between plateau and linear SNe II.
2. The difference between absolute magnitudes of two SNe is given by

$$M_{1,i} - M_{2,i} = 5\log\left(\frac{v_{\mathrm{ph},2,i}}{v_{\mathrm{ph},1,i}}\right). \tag{37}$$

In the case of a typical SN II-P (such as SN 2004et), $v_{\mathrm{ph}} \sim 4000\,\mathrm{km\,s^{-1}}$ at the middle of the plateau. There are, however, II-P events characterized by low expansion velocities and low luminosities, which are known as subluminous SNe II-P (Pastorello et al. 2004; Spiro et al. 2014). These events are characterized by expansion velocities of the order of $v_{\mathrm{ph}} \sim 1500\,\mathrm{km\,s^{-1}}$ at the middle of the plateau. From Equation (37), subluminous events should be ∼2 mag fainter than typical SNe II-P.

To test the above points, we need more than four well-observed SNe. Also we need to include linear and subluminous events. In order to compute absolute magnitudes using redshift-based distances, we select 14 SNe from our set, of which 4 are linear (SN 1991al, SN 2003ci, SN 2003hk, and SN 2003ip) and 1 is subluminous with low expansion velocities (SN 2003bl); all of them are within the Hubble flow, i.e., $cz_{\mathrm{CMB}} > 3000\,\mathrm{km\,s^{-1}}$, where cz_{CMB} is the host galaxy redshift in the cosmic microwave background frame. They also have at least three spectroscopic

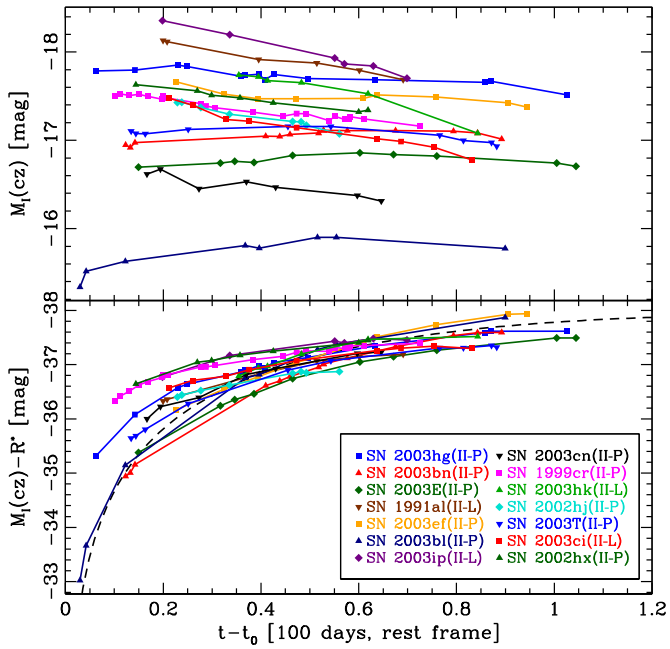

Figure 9. Top: *I*-band absolute light curves in the rest frame of 14 SNe II within the Hubble flow and with at least three spectroscopic observations. Bottom: photospheric light curves for the same SNe and the relation obtained from our nearby SNe (dashed line). SN names are sorted by increasing redshift.

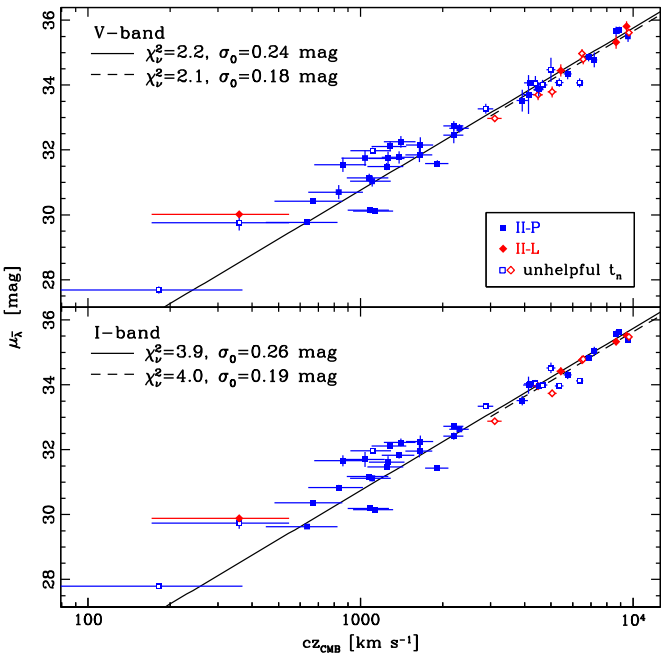

Figure 10. Hubble diagram for our SN set, using parameters derived in this work. Solid lines represent linear fits using all SNe in our set and dashed lines represent linear fits using only SNe with $cz_{\rm CMB} > 3000\,{\rm km\,s^{-1}}$.

observations in order to perform a power-law fit (Equation (33)) to the expansion velocities and estimate the $\mathcal{R}$-term for each photometric point.

The top panel of Figure 9 shows the *I*-band absolute light curves of 14 SNe II within the Hubble flow using $H_0 = 72\,{\rm km\,s^{-1}}$ Mpc^{-1}. The spread between fainter and brighter events is of ∼2.5 mag. The bottom of Figure 9 shows the *I*-band photospheric light curves. We see that SNe are located approximately on the same locus as our nearby SNe (dashed line), independent of whether they are plateau, linear, or subluminous events. The largest dispersion occurs before ∼40 days and is probably due to the uncertainty in the shock breakout epoch and the scarcity of early spectroscopic observations. In the range of 50–90 days the spread between fainter and brighter events is ⩽0.6 mag. Figure 9 illustrates that the apparent diversity of slopes and magnitudes of SN II light curves during the photospheric phase is linked with the velocity profile of SNe.

5.2.3. Photospheric Magnitude Method

Working with redshift instead of distance modulus in Equation (31), we obtain

$$m^{\rm corr}_{\bar{\lambda},i} - A_h(\bar{\lambda}) + 5\log(v_{{\rm ph},i}) = 5\log(cz) + \mathcal{M}^*_{\bar{\lambda},i} - 5\log(H_0 100\ {\rm days}), \quad (38)$$

where H_0 is the Hubble constant. For an epoch t_p at the middle of the plateau (e.g., 50 days since shock breakout), Equation (38) reduces to the original version of the standardized candle method (SCM) proposed by Hamuy & Pinto (2002), i.e.,

$$m^{\rm corr}_{\bar{\lambda},p} - A_h(\bar{\lambda}) + \alpha\log(v_{{\rm ph},p}) = 5\log(cz) + zp, \quad (39)$$

where α and zp are free parameters to fit from the observations by minimizing the dispersion in the Hubble diagram. In Equation (38) $\alpha = 5$ as a consequence of assuming spherical symmetry and $zp = \mathcal{M}^*_{\bar{\lambda},i} - 5\log(H_0 100\ {\rm days})$, which is constant for a fixed time. So, Equation (31) corresponds to the generalization of the SCM for various epochs throughout the photospheric phase. Hereafter we will refer to it as the photospheric magnitude method (PMM).

Most recent versions of the SCM (e.g., Poznanski et al. 2009; D'Andrea et al. 2010) use

$$A_h(\bar{\lambda}) = R_{\bar{\lambda},V-I}(R_V)[(V-I)_p - (V-I)_{0,p}], \quad (40)$$

where $(V-I)_p$ is the color measured at t_p and $(V-I)_{0,p}$ is the (supposed) intrinsic color at the same epoch. The reasons to use Equation (40) in Equation (39) are avoiding calculation of the value of $(V-I)_{0,p}$ (essential for the reddening determination), which is absorbed by zp, and using the SCM to determine R_V (i.e., a third parameter to adjust to the observations). In the case of the PMM, the incorporation of Equation (40) in Equation (38) is inaccurate because it is equivalent to supposing that all SNe II have the same intrinsic color curve $(V-I)_{0,i}$. So, in order to use the PMM, we necessarily require knowledge of the host galaxy extinction with the most appropriate value of R_V for SNe II.

5.2.4. Application: The Hubble Constant

For an SN with measured observables $\{m^{\rm corr}_{\bar{\lambda}}, v_{\rm ph}\}$, $A_h(\bar{\lambda})$ and t_0, with photometric and spectroscopic data at the same epoch, we can calculate the distance modulus using the PMM via

$$\mu_{\bar{\lambda}} = \left\langle m^{\rm corr}_{\bar{\lambda},i} - \mathcal{R}^*(v_{{\rm ph},i}) - \mathcal{M}^*_{\bar{\lambda},i}(t_0)\right\rangle - A_h(\bar{\lambda}), \quad (41)$$

$$\sigma^2_{\mu_{\bar{\lambda}}} = \sigma^2_{\langle m^{\rm corr}_{\bar{\lambda},i} - \mathcal{R}^*(v_{{\rm ph},i})\rangle} + \sigma^2_{A_h(\bar{\lambda})}. \quad (42)$$

Table 5 shows our results for the *V* and *I* bands, where we use the midpoint time as the shock breakout epoch. A direct way to test the previous results is through the construction of a Hubble diagram. Figure 10 shows the Hubble diagram using *V* (top) and *I* (bottom) bands. To obtain the Hubble constant and the intrinsic dispersion σ_0, we maximize the marginal likelihood function $\mathcal{L}$

Table 5
Hubble Diagram SNe Sample

Host Galaxy[a]	cz_{CMB}[b] (km s^{-1})	SN Name	SN Type[c]	$\mu_V(\sigma)$ (mag)	$\mu_I(\sigma)$ (mag)
NGC 6946	−141	2004et	II-P	28.65(0.08)	28.73(0.05)
NGC 2403	182	2004dj	II-P	27.68(0.11)	27.79(0.05)
NGC 628	359	2003gd	II-P	29.76(0.24)	29.74(0.18)
		2013ej	II-L	30.01(0.07)	29.88(0.05)
NGC 5194	636	2005cs	II-P	29.77(0.08)	29.63(0.05)
NGC 1637	670	1999em	II-P	30.42(0.06)	30.36(0.03)
NGC 3184	831	1999gi	II-P	30.70(0.22)	30.83(0.09)
NGC 6207	862	2004A	II-P	31.54(0.22)	31.66(0.17)
NGC 3938	1038	2005ay	II-P	31.75(0.24)	31.70(0.23)
UGC 2890	1077	2009bw	II-P	31.14(0.13)	31.17(0.08)
NGC 3239	1084	2012A	II-P	30.14(0.09)	30.19(0.05)
NGC 1448	1102	2003hn	II-P	31.04(0.17)	31.12(0.09)
NGC 1097	1105	2003B	II-P	31.98(0.09)	31.97(0.05)
NGC 3351	1127	2012aw	II-P	30.12(0.09)	30.15(0.05)
NGC 2082	1246	1992ba	II-P	31.49(0.11)	31.47(0.07)
NGC 918	1261	2009js	II-P	31.74(0.21)	31.62(0.18)
NGC 4900	1285	1999br	II-P	32.11(0.15)	32.11(0.07)
NGC 4487	1386	2009N	II-P	31.77(0.19)	31.83(0.10)
NGC 2742	1405	2003Z	II-P	32.25(0.18)	32.22(0.12)
NGC 5921	1646	2001X	II-P	31.85(0.22)	31.96(0.20)
NGC 3389	1656	2009md	II-P	32.15(0.24)	32.25(0.19)
NGC 4303	1913	2008in	II-P	31.58(0.10)	31.43(0.07)
NGC 772	2198	2003hl	II-P	32.46(0.25)	32.42(0.11)
		2003iq	II-P	32.74(0.15)	32.72(0.07)
NGC 7537	2304	2002gd	II-P	32.67(0.13)	32.63(0.06)
NGC 922	2879	2002gw	II-P	33.27(0.15)	33.34(0.06)
NGC 3120	3108	1999ca	II-L	32.97(0.10)	32.88(0.07)
NGC 7771	3921	2003hg	II-P	33.52(0.34)	33.51(0.14)
ESO 235–G58	4134	2003ho	II-P	33.71(0.60)	33.99(0.26)
2MASX J10023529–2110531	4172	2003bn	II-P	34.07(0.07)	34.03(0.04)
MCG –04–12–004	4380	2003E	II-P	34.05(0.23)	34.05(0.10)
anon	4484[d]	1991al	II-L	33.70(0.17)	33.96(0.07)
NGC 4708	4504	2003ef	II-P	33.87(0.22)	33.96(0.10)
NGC 5374	4652	2003bl	II-P	34.00(0.16)	33.99(0.09)
UGC 11522	4996	2003fb	II-P	34.47(0.37)	34.52(0.16)
UGC 327	5050	2003ip	II-L	33.79(0.17)	33.74(0.10)
ESO 340–G38	5359	1992af	II-P	34.08(0.13)	33.97(0.07)
UGC 7820	5431	2003ej	II-L	34.45(0.19)	34.42(0.12)
IC 849	5753	2003cn	II-P	34.34(0.16)	34.31(0.13)
ESO 576–G34	6363	1999cr	II-P	34.07(0.14)	34.12(0.06)
IC 1861	6494	1999eg	II-L	34.97(0.14)	34.77(0.13)
NGC 1085	6568	2003hk	II-L	34.80(0.16)	34.79(0.08)
NPM1G +04.0097	6869	2002hj	II-P	34.85(0.12)	34.82(0.05)
MCG –04–48–015	7203	2003ib	II-P	34.78(0.23)	35.03(0.14)
UGC 4864	8662	2003T	II-P	35.65(0.15)	35.58(0.10)
NEAT J205430.50–000822.0	8671	2002ew	II-L	35.32(0.20)	35.33(0.11)
2MASX J07391822–6203095	8908	1993A	II-P	35.69(0.11)	35.62(0.08)
UGC 6212	9468	2003ci	II-L	35.81(0.16)	35.51(0.09)
2MASX J08273975–1446551	9573	2002hx	II-P	35.50(0.17)	35.38(0.08)
2MASX J22522390–4018432	9645	1993S	II-L	35.62(0.10)	35.48(0.06)

Notes. Distance moduli are computed using the midpoint time as the shock breakout epoch. Uncertainties do not include the intrinsic scatter of the PMM.
[a] Sorted by increasing redshift.
[b] Values from the NASA/IPAC Extragalactic Database, unless otherwise noted, with an error of 187 km s^{-1} due to the uncertainty in the determination of the Local Group velocity.
[c] Old SN subclassification based on the B-band decline rate (β^B_{100}) criterion given in Patat et al. (1994).
[d] Hamuy (2001).

minimizing the quantity

$$-2\ln\mathcal{L} = \sum_{SN}\left\{\ln V + \frac{(\mu - (25 - 5\log H_0) - 5\log cz_{CMB})^2}{V}\right\}, \quad (43)$$

$$V = \sigma_\mu^2 + \left(\frac{5}{\ln 10}\frac{\sigma_{cz_{CMB}}}{cz_{CMB}}\right)^2 + \sigma_0^2 \quad (44)$$

(e.g., Kelly 2007), where the summation is over all the SNe in our sample. For the V and I bands we obtain an intrinsic dispersion of 0.24–0.26 mag, indicating a relative distance scatter of 12%.

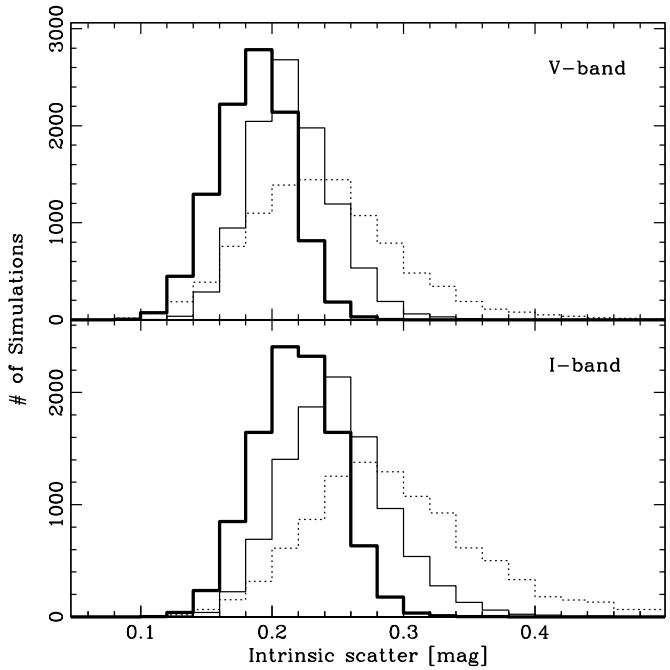

Figure 11. Histograms showing the intrinsic scatter in the V (top) and I (bottom) bands, performing Monte Carlo simulations for the shock breakout epoch in the ranges $t_m - \Delta t < t_0 < t_m + \Delta t$ (dotted line), $t_m < t_0 < t_m + \Delta t$ (thin line), and $t_m - \Delta t < t_0 < t_m$ (thick line).

Using only SNe within the Hubble flow, the intrinsic scatter is reduced to 0.18–0.19 mag, indicating a relative distance scatter of 8%–9%.

The mean uncertainty in the shock breakout epoch for our 24 SNe in the Hubble flow is six days, so the choice of t_0 may have an important effect on the intrinsic scatter. Figure 11 shows the results of Monte Carlo simulations for t_0 in the range $t_m - \Delta t < t_0 < t_m + \Delta t$ (dotted line). The intrinsic scatter is around 0.24 and 0.28 mag for V (top) and I (bottom) bands, respectively, values greater than our previous results. To study the contribution of the shock breakout epoch uncertainty to the intrinsic scatter, we divide the range where t_0 lies into two: $t_m - \Delta t < t_0 < t_m$ (lower range) and $t_m < t_0 < t_m + \Delta t$ (upper range). Figure 11 shows the results of Monte Carlo simulations for t_0 in the lower range (thick line) and in the upper range (thin line). Both ranges yield lower values for the intrinsic scatter than the values obtained with the entire range. However, the best results are obtained with the lower limit, with an intrinsic scatter of 0.19–0.22 mag. This may be because, in general, our 24 SNe in the Hubble flow were first detected after maximum light, so the shock breakout occurred, in fact, several days before the first detection. So choosing the lower limit can correct for this systematic error.

The similarity between the results obtained with t_m as t_0, and those obtained with t_0 in the range $t_m - \Delta t < t_0 < t_m$ means an uncertainty of three days in the shock breakout epoch does not produce an important contribution to the intrinsic scatter.

We repeat the previous analysis using the 13 SNe in the Hubble flow with the shock breakout epoch estimated using nondetection. With the aforementioned correction of the shock breakout epoch, we obtain a mean intrinsic scatter of 0.12 mag, or 6% in relative distances. Also we obtain $H_0 = 68$–69 km s^{-1} Mpc^{-1}. This value is based on the calibration obtained with our nearby SNe (Figure 7), which in turn is based on the Saha et al. (2006) calibration ($\mu_{\rm LMC} = 18.54$ mag).

6. DISCUSSION

6.1. The C3 Method

Reddening measurements using the C3(BVI) method have a systematic uncertainty, mostly due to line blanketing, that affects the SNe II B band after maximum light so, despite the good agreement between reddening from the C3(BVI) method and from the spectroscopic analysis, it will be necessary to take into account the effect that metallicity has over reddening measurements in order not to propagate this effect to the V and I bands. Another source of uncertainty is the difference between photometric systems, so future works will need to consider the application of the S-correction (Stritzinger et al. 2002).

6.2. SBM for SNe II

The SBM has been used successfully in Cepheid distance measurements with subsequent calibration of the Cepheid period–luminosity relation (e.g., Storm et al. 2011). The calibration of the SBM is made possible by the current ability to measure angular diameters of Galactic Cepheids through interferometric observations (Welch 1994; Kervella et al. 2004b). In the case of SNe II, interferometric observations are possible only for the nearest events through very long baseline interferometry, while indirect measurements of the angular sizes require the knowledge of expansion velocities, the shock breakout epoch, and the distance to the SN. The complex scenario for SNe II was probably the reason why astronomers chose to use methods based on models, such as the EPM, instead of calibrating the SBM for SNe II.

Kasen & Woosley (2009) suggest that the SBM for SNe II is used through the SCM, arguing that the temperature in the middle of the plateau is nearly constant. In addition, using SN II models, they find a relation between absolute magnitude and photospheric velocity during the plateau phase similar to our Equation (34), in which we include a linear term for modeling linear events. We remark that the SBM relates the surface brightness with a color index and not with time. Thus the result obtained by Kasen & Woosley (2009) is the first attempt at a time-based standardization for SNe II, of which our work is an empirical proof.

6.3. The Future of the PMM

Based on our results, the PMM can replace the SCM, the latter being only a special case. This is an important improvement because, unlike the SCM, we will have not one but several points for each SN, depending on the number of observations we have and the interpolation we use. So we can obtain more accurate results as more photometric and spectroscopic data are available. In our case, the observational uncertainty (first term of Equation (42)) is reduced with the number of spectroscopic observations. Also with more photometric observations, we can reduce the host galaxy extinction uncertainty (the second term of Equation (42)).

In order to reduce the uncertainty produced by the estimated shock breakout epoch, we need constrain it to a range of one week. This requirement was previously achieved in SN samples used by Poznanski et al. (2009) and D'Andrea et al. (2010). It will be important that future surveys for SNe II take into account this constraint.

Based on the resulting dispersion, our work shows that the most promising method for measuring distances to SNe II is not the SBM (Figure 6) but the PMM (Figures 7 and 9).

In a future work we will investigate the possible application of the SBM and the PMM to other SN classes during their photospheric phase.

7. CONCLUSIONS

In this work we tested improved ways of estimating distances using SNe II. We found a temperature-dependent quantity that we call "photospheric magnitude," which is equivalent to the surface brightness previously used for Cepheid distance measurements through its relation to a suitable color index. To study the applicability of the method, we use 50 SNe II with redshifts lower than 10^4 km s^{-1}, and with photometric and spectroscopic data during the photospheric phase. We also develop a method for measuring host galaxy extinctions, equivalent to that proposed by Natali et al. (1994) for open clusters. Our main conclusions are the following.

1. $B-V$ versus $V-I$ color–color curves provide us with the possibility of measuring reddening. The comparison between reddenings from spectroscopic analysis and from the C3(BVI) method is satisfactory within the errors of both techniques.
2. We construct a color–magnitude diagram (CMD) using our nearby SNe. All of them are in galaxies with distances measured with Cepheids and with an uncertainty in the shock breakout epoch smaller than a few days. The CMD shows a linear relation with a dispersion of 0.29 mag, which represents a scatter in relative distances of 13%.
3. Using time since shock breakout instead of color as the independent variable, the above relation turns into a photospheric light curve. We identify it as the generalization of the SCM for various epochs throughout the photospheric phase. The dispersion of 0.09 mag represents a scatter in relative distances of 4%.
4. The diversity of slopes and magnitudes of SN II light curves during the photospheric phase is mostly produced by the expansion velocity evolution of each SN.
5. Finally, we applied the time-based standardization to our SN set in order to calculate their distances and to construct a Hubble diagram. Using only SNe within the Hubble flow with well-constrained shock breakout epochs, we obtain $H_0 = 68$–69 km s^{-1} Mpc^{-1}. The mean intrinsic dispersion of 0.12 mag represents a scatter in relative distances of 6%. It confirms the low intrinsic dispersion of the method.

We acknowledge support by projects IC120009 "Millennium Institute of Astrophysics (MAS)," P10-064-F "Millennium Center for Supernova Science" of the Iniciativa Científica Milenio del Ministerio Economía, Fomento y Turismo de Chile, and by projects FONDAP 15010003, ALMA-CONICYT 31110008, and BASAL PFB-06 of CONICYT. This research has made use of the NASA/IPAC Extragalactic Database (NED) which is operated by the Jet Propulsion Laboratory, California Institute of Technology, under contract with the National Aeronautics and Space Administration. This work has made use of the Weizmann Interactive Supernova Repository (http://www.weizmann.ac.il/astrophysics/wiserep). A preliminary version of this work (Rodríguez 2013) was developed as a Masters thesis.

REFERENCES

Anderson, J. P., González-Gaitn, S., Hamuy, M., et al. 2014, ApJ, 786, 67
Baade, W. 1926, AN, 228, 359
Barbon, R., Ciatti, F., & Rosino, F. 1979, A&A, 72, 287
Barnes, T. G., & Evans, D. S. 1976, MNRAS, 174, 489
Blondin, S., & Tonry, J. L. 2007, ApJ, 666, 1024
Bose, S., & Kumar, B. 2014, ApJ, 782, 98
Bose, S., Kumar, B., Sutaria, F., et al. 2013, MNRAS, 433, 1871
Burrows, A. 2000, Natur, 403, 727
Cardelli, J. A., Clayton, G. C., & Mathis, J. S. 1989, ApJ, 345, 245
Cleveland, W. S., Grosse, E., & Shyu, M. J. 1992, in Statistical Models in S, ed. J. M. Chambers & T. J. Hastie (London: Chapman and Hall), 309
Cousins, A. W. J. 1971, ROAn, 7, 86
Dall'Ora, M., Botticella, M. T., Pumo, M. L., et al. 2014, ApJ, 787, 139
D'Andrea, C. B., Sako, M., Dilday, B., et al. 2010, ApJ, 708, 661
Dessart, L., Blondin, S., Brown, P. J., et al. 2008, ApJ, 675, 644
Dessart, L., Gutierrez, C. P., Hamuy, M., et al. 2014, MNRAS, 440, 1856
Dessart, L., & Hillier, D. J. 2005, A&A, 437, 667
Dessart, L., & Hillier, D. J. 2006, A&A, 447, 691
Eastman, R. G., Schmidt, B. P., & Kirshner, R. 1996, ApJ, 466, 911
Filippenko, A. V. 1982, PASP, 94, 715
Fitzpatrick, E. L. 1999, PASP, 111, 63
Fouqué, P., & Gieren, W. P. 1997, A&A, 320, 799
Fraser, M., Ergon, M., Eldridge, J. J., et al. 2011, MNRAS, 417, 1417
Gandhi, P., Yamanaka, M., Tanaka, M., et al. 2013, ApJ, 767, 166
Hamuy, M. 2001, PhD thesis, Univ. Arizona
Hamuy, M., Folatelli, G., Morrell, N. I., et al. 2006, PASP, 118, 2
Hamuy, M., Phillips, M. M., Suntzeff, N. B., et al. 1996, AJ, 112, 2391
Hamuy, M., & Pinto, P. A. 2002, ApJL, 566, L63
Hamuy, M., Pinto, P. A., Maza, J., et al. 2001, ApJ, 558, 615
Hamuy, M., Suntzeff, N. B., Heathcote, S. R., et al. 1994, PASP, 106, 566
Hamuy, M., Walker, A. R., Suntzeff, N. B., et al. 1992, PASP, 104, 533
Harutyunyan, A. H., Pfahler, P., Pastorello, A., et al. 2008, A&A, 488, 383
Hendry, M. A., Smartt, S. J., Crockett, R. M., et al. 2006, MNRAS, 369, 1303
Inserra, C., Turatto, M., Pastorello, A., et al. 2012, MNRAS, 422, 1122
Johnson, H. L., Mitchell, R. I., Iriarte, B., & Wisniewski, W. Z. 1966, CoLPL, 4, 99
Jones, M. I. 2008, MSc thesis, Univ. de Chile (arXiv:0810.5538)
Jones, M. I., Hamuy, M., Lira, P., et al. 2009, ApJ, 696, 1176
Kasen, D., & Woosley, S. E. 2009, ApJ, 703, 2205
Kelly, B. C. 2007, ApJ, 665, 1489
Kervella, P., Bersier, D., Mourard, D., et al. 2004a, A&A, 428, 587
Kervella, P., Nardetto, N., Bersier, D., Mourard, D., & Coudé du Foresto, V. 2004b, A&A, 416, 941
Kirshner, R. P., & Kwan, J. 1974, ApJ, 193, 27
Kleiser, I. K. W., Poznanski, D., Kasen, D., et al. 2011, MNRAS, 415, 372
Landolt, A. U. 1992, AJ, 104, 340
Leonard, D. C., Filippenko, A. V., Gates, E. L., et al. 2002a, PASP, 114, 35
Leonard, D. C., Filippenko, A. V., Li, W., et al. 2002b, AJ, 124, 2490
Li, W., Filippenko, A. V., Treffers, R. R., et al. 2001, ApJ, 546, 734
Li, W., Leaman, J., Chornock, R., et al. 2011, MNRAS, 412, 1441
Maguire, K., Di Carlo, E., Smartt, S. J., et al. 2010, MNRAS, 404, 981
Minkowski, R. 1941, PASP, 53, 224
Misra, K., Pooley, D., Chandra, P., et al. 2007, MNRAS, 381, 280
Munari, U., & Carraro, G. 1996, A&A, 314, 108
Natali, F., Natali, G., Pompei, E., & Pedichini, F. 1994, A&A, 289, 756
O'Donnell, J. 1994, ApJ, 422, 158
Olivares, F., Hamuy, M., Pignata, G., et al. 2010, ApJ, 715, 833
Pastorello, A., Pumo, M. L., Navasardyan, H., et al. 2012, A&A, 537, A141
Pastorello, A., Sauer, D., Taubenberger, S., et al. 2006, MNRAS, 370, 1752
Pastorello, A., Valenti, S., Zampieri, L., et al. 2009, MNRAS, 394, 2266
Pastorello, A., Zampieri, L., Turatto, M., et al. 2004, MNRAS, 347, 74
Patat, F., Barbon, R., Cappellaro, E., & Turatto, M. 1994, A&A, 282, 731
Phillips, M. M. 1993, ApJL, 413, L105
Phillips, M. M., Lira, P., Suntzeff, N. B., et al. 1999, AJ, 118, 1766
Poznanski, D., Butler, N., Filippenko, A. V., et al. 2009, ApJ, 694, 1067
Poznanski, D., Prochaska, J. X., & Bloom, J. S. 2012, MNRAS, 426, 1465
Press, W. H., Teukolsky, S. A., Vetterling, W. T., & Flannery, B. P. 1992, Numerical Recipes in FORTRAN (2d ed.; New York: Cambridge Univ. Press)
Richmond, M. W. 2014, JAVSO, in press (arXiv:1405.7900)
Rodríguez, Ó 2013, MSc thesis, Pontificia Universidad Católica de Chile
Roy, R., Kumar, B., Benetti, S., et al. 2011, ApJ, 736, 76
Saha, A., Thim, F., Tammann, G. A., Reindl, B., & Sandage, A. 2006, ApJS, 165, 108
Sahu, D. K., Anupama, G. C., Srividya, S., & Muneer, S. 2006, MNRAS, 372, 1315
Schlafly, E. F., & Finkbeiner, D. P. 2011, ApJ, 737, 103
Schlegel, E. M. 1990, MNRAS, 244, 269
Schmidt, B. P., Kirshner, R. P., & Eastman, R. G. 1992, ApJ, 395, 366

Schmidt, B. P., Kirshner, R. P., Eastman, R. G., et al. 1994, AJ, 107, 1444
Schneider, D. P., Gunn, J. E., & Hoessel, J. G. 1983, ApJ, 264, 337
Smartt, S. J. 2009, ARA&A, 47, 63
Smith, N., Li, W., Filippenko, A. V., & Chornock, R. 2011, MNRAS, 412, 1522
Spiro, S., Pastorello, A., Pumo, M. L., et al. 2014, MNRAS, 439, 2873
Storm, J., Gieren, W., Fouqué, P., et al. 2011, A&A, 534, A94
Stritzinger, M., Hamuy, M., Suntzeff, N. B., et al. 2002, AJ, 124, 2100
Taddia, F., Stritzinger, M. D., Sollerman, J., et al. 2012, A&A, 537, A140
Takáts, K., Pumo, M. L., Elias-Rosa, N., et al. 2014, MNRAS, 438, 368
Tomasella, L., Cappellaro, E., Fraser, M., et al. 2013, MNRAS, 434, 1636
Tsvetkov, D. Y. 2006, PZ, 26, 3
Tsvetkov, D. Y. 2008, PZ, 28, 3
Tsvetkov, D. Y., Goranskiy, V. P., & Pavlyuk, N. N. 2008, PZ, 28, 8
Tsvetkov, D. Y., Volnova, A. A., Shulga, A. P., et al. 2006, A&A, 460, 769
Tully, B. 1988, Nearby Galaxies Catalog (New York: Cambridge Univ. Press)
Valenti, S., Sand, D., Pastorello, A., et al. 2014, MNRAS, 438, L101
Van Dyk, S. D., Li, W., & Filippenko, A. V. 2003, PASP, 115, 1289
Vinkó, J., Takáts, K., Sárneczky, K., et al. 2006, MNRAS, 369, 1780
Wagoner, R. V. 1981, ApJL, 250, L65
Welch, D. L. 1994, AJ, 108, 1421
Wesselink, A. J. 1969, MNRAS, 144, 297
Woosley, S. E., Pinto, P. A., Martin, P. G., & Weaver, T. A. 1987, ApJ, 318, 664
Yaron, O., & Gal-Yam, A. 2012, PASP, 124, 668